


Arc self-association and formation of virus-like capsids are mediated by an N-terminal helical coil motif

Maria S. Eriksen^{1,2} , Oleksii Nikolaienko^{1,2} , Erik I. Hallin¹, Sverre Grødem^{1,2}, Helene J. Bustad^{1,2} , Marte I. Flydal^{1,2} , Ian Merski³, Tomohisa Hosokawa⁴ , Daniela Lascu^{1,2}, Shreeram Akerkar^{1,2}, Jorge Cuéllar⁵, James J. Chambers⁶, Rory O'Connell³, Gopinath Muruganandam^{7,8} , Remy Loris^{7,8} , Christine Touma⁹, Tambudzai Kanhema^{1,2}, Yasunori Hayashi⁴ , Margaret M. Stratton³, José M. Valpuesta⁵, Petri Kursula^{1,9} , Aurora Martinez^{1,2}  and Clive R. Bramham^{1,2} 

- 1 Department of Biomedicine, University of Bergen, Norway
- 2 KG Jebsen Centre for Neuropsychiatric Disorders, University of Bergen, Norway
- 3 Department of Biochemistry and Molecular Biology, University of Massachusetts Amherst, MA, USA
- 4 Department of Pharmacology, Kyoto University Graduate School of Medicine, Kyoto, Japan
- 5 Centro Nacional de Biotecnología (CNB-CSIC), Madrid, Spain
- 6 Institute for Applied Life Sciences, University of Massachusetts Amherst, MA, USA
- 7 VIB-VUB Center for Structural Biology, Vlaams Instituut voor Biotechnologie, Brussels, Belgium
- 8 Structural Biology Brussels, Department of Bioengineering Sciences, Vrije Universiteit Brussel, Belgium
- 9 Faculty of Biochemistry and Molecular Biology & Biocenter Oulu, University of Oulu, Finland

Keywords

activity-regulated cytoskeleton-associated protein (Arc)/coiled-coil interactions/protein oligomerization; retrovirus-like capsid/synaptic plasticity

Correspondence

C. R. Bramham, Department of Biomedicine, University of Bergen, 5009 Bergen, Norway
Tel: +47 48125046
Email: clive.bramham@uib.no

S-SAD phasing data: Hallin, Erik I., Touma, Christine, Bramham, Clive R., & Kursula, Petri. (2020). S-SAD dataset for solving the structure of the Arc dimerisation motif [Data set]. Zenodo. <http://doi.org/10.5281/zenodo.3765570>
High-resolution native data: Hallin, Erik I., Touma, Christine, Bramham, Clive R., & Petri Kursula. (2020). High-resolution X-ray diffraction dataset for the coiled-coil

Activity-regulated cytoskeleton-associated protein (Arc) is a protein interaction hub with diverse roles in intracellular neuronal signaling, and important functions in neuronal synaptic plasticity, memory, and postnatal cortical development. Arc has homology to retroviral Gag protein and is capable of self-assembly into virus-like capsids implicated in the intercellular transfer of RNA. However, the molecular basis of Arc self-association and capsid formation is largely unknown. Here, we identified a 28-amino-acid stretch in the mammalian Arc N-terminal (NT) domain that is necessary and sufficient for self-association. Within this region, we identified a 7-residue oligomerization motif, critical for the formation of virus-like capsids. Purified wild-type Arc formed capsids as shown by transmission and cryo-electron microscopy, whereas mutant Arc with disruption of the oligomerization motif formed homogenous dimers. An atomic-resolution crystal structure of the oligomerization region peptide demonstrated an antiparallel coiled-coil interface, strongly supporting NT-NT domain interactions in Arc oligomerization. The NT coil-coil interaction was also validated in live neurons using fluorescence lifetime FRET imaging, and mutation of the oligomerization motif disrupted Arc-facilitated endocytosis. Furthermore, using single-molecule photobleaching, we show that Arc mRNA greatly enhances higher-order oligomerization in a manner dependent on the oligomerization motif. In conclusion, a helical coil in the Arc

Abbreviations

Arc, activity-regulated cytoskeleton-associated protein; Arc 3.1, activity-regulated gene 3.1; dArc, Drosophila Arc; CA, capsid domain; CD, circular dichroism; CT, C-terminal; DLS, dynamic light scattering; EM, electron microscopy; EGFP, enhanced green fluorescent protein; FLIM, fluorescence lifetime imaging; FRET, Förster resonance energy transfer; Gag, group-specific antigen; LTD, long-term depression; LTP, long-term potentiation; MA, matrix domain; MALS, multi-angle light scattering; MBP, maltose-binding protein; mCh, mCherry; mTq2, mTurquoise2; NC, nucleocapsid domain; NT, N-terminal; SAXS, small-angle X-ray scattering; SEC, size-exclusion chromatography; smTIRF, single-molecule total internal reflection microscopy; SAD, single-wavelength anomalous dispersion; WT, wild-type.

oligomerization domain of human Arc [Data set]. Zenodo. <http://doi.org/10.5281/zenodo.3766064>

(Received 3 September 2020, revised 13 October 2020, accepted 26 October 2020)

doi:10.1111/febs.15618

NT domain supports self-association above the dimer stage, mRNA-induced oligomerization, and formation of virus-like capsids.

Database

The coordinates and structure factors for crystallographic analysis of the oligomerization region were deposited at the Protein Data Bank with the entry code [6YTU](#).

Introduction

Activity-regulated cytoskeleton-associated protein (Arc), also known as activity-regulated gene 3.1 (Arg3.1), has emerged as a key regulator of neuronal plasticity, memory, and postnatal cortical development [1–3]. Arc is induced as an immediate early gene, and the neuronal activity-induced Arc mRNA and protein are subject to rapid turnover, indicating a highly dynamic mode of action. Loss-of-function studies support a role for Arc in long-term potentiation (LTP) and long-term depression (LTD) of synaptic transmission and homeostatic synaptic scaling. These diverse responses are mediated by distinct Arc protein–protein interaction complexes in the postsynaptic dendritic compartment and the neuronal nucleus [4–9]. Thus, convergent lines of evidence support a role for Arc as a signaling hub protein and cell-autonomous organizer of synaptic plasticity [10].

The mechanisms that dictate Arc function at the molecular level are poorly understood. Post-translational modification of Arc by SUMOylation [8,11] and ERK-catalyzed phosphorylation [12] are implicated in the regulation of protein–protein interactions and subcellular localization, while Arc turnover is regulated by ubiquitination, acetylation, and GSK-catalyzed phosphorylation [13–17]. In addition, recombinant Arc is capable of reversible self-association [18,19]. Purified human Arc forms higher-order oligomeric species, dependent on ionic strength, but reverses to monomers and dimers at low ionic strength [19]. This reversible oligomerization raised the possibility that Arc function is determined by its oligomeric state.

Recent advances highlight a structural and functional relationship between Arc and retroviral Gag polypeptide. Arc was identified in a computational search for domesticated retrotransposons harboring Gag-like protein domains [20]. Biochemical studies showed that mammalian Arc has a positively charged N-terminal (NT) domain and a negatively charged C-terminal (CT) domain, separated by a flexible linker [19]. Crystal structure analysis of the isolated CT

domain revealed two lobes, both with striking 3D homology to the capsid (CA) domain of HIV Gag [9,21]. In retroviruses, self-association of CA allows assembly of Gag polypeptides into the immature capsid shell [22,23]. Remarkably, recombinant Arc from fruit fly and rat was shown to self-assemble into spherical particles resembling retroviral Gag capsids [24,25]. Arc capsids are released in extracellular vesicles and are capable of transmitting RNA cargo to recipient cells [24,25], indicating a new, non-cell autonomous role for Arc as an endogenous neuronal retrovirus [26,27].

Interestingly, while tetrapod species (mammals, birds, reptiles, and amphibians) and *Drosophila* both have a CA-like domain, the large NT domain is a unique feature of tetrapod evolution [9,25,28,29]. The structure and function of the Arc NT domain are poorly known, but the region is expected to have evolved from the N-terminal, matrix (MA) domain of the Gag polypeptide [20]. Like retroviral MA [30], the Arc NT domain mediates binding to phospholipid membranes [31,32]. However, unlike retroviral MA [33], the Arc NT domain is predicted to have an antiparallel coiled-coil structure [31].

Here, we sought to elucidate the molecular basis of mammalian Arc self-association and capsid formation. We identified a 28-amino-acid stretch, termed the oligomerization region, which is both necessary and sufficient for oligomerization. The oligomerization region is located in predicted Coil-2 of the Arc NT domain. Within this region, we identified a critical 7-residue oligomerization motif. Crystal structure analysis of a synthetic oligomerization region peptide showed formation of an antiparallel, helical coiled-coil, strongly supporting NT-NT domain interactions in Arc oligomerization. Electron microscopy (EM) and small-angle X-ray scattering (SAXS) analysis of purified protein showed that wild-type (WT) Arc forms virus-like capsids, whereas the oligomerization motif mutant is dimeric. Using single-molecule photobleaching, we show that Arc mRNA greatly enhances oligomerization in a manner dependent on the

oligomerization motif. Thus, an NT domain helical coil is critical for Arc self-association, mRNA-induced oligomerization, and capsid formation.

Results

Arc self-association is mediated by N-terminal domain Coil-2

First, we sought to map the regions of Arc-mediating oligomerization using a stringent affinity purification assay. We coexpressed two variants of Arc in a human embryonic kidney cell line (HEK293FT): (1) Arc with an N-terminal fusion to mTurquoise2 (mTq2) and (2) Arc with a C-terminal fusion to StrepII tag (Fig. 1A). Next, mTq2-fused full-length Arc (1–396) was coprecipitated with StrepII-tagged Arc, indicating complex formation (Fig. 1C). Specificity was confirmed by the absence of mTq2-positive bands in purifications from cells transfected with StrepII-Arc and the empty mTq2 vector. Arc contains five cysteine residues (Cys34, Cys94, Cys96, Cys98, and Cys159), which might form disulfide-linked oligomeric species. However, substituting all five cysteines with serines did not affect the Arc-Arc interaction, showing that oligomerization does not require disulfide bond formation (Fig. 1C). We next coexpressed truncated versions of Arc fused to mTq2 to determine the minimal regions needed for association (Fig. 1B,D). When StrepII-tagged full-length Arc was coexpressed with mTq2-fused N-terminal region (1–140), linker (135–216), or C-terminal region (208–396), only the N-terminal region showed binding (Fig. 1D). The involvement of the N-terminal region in self-association agrees with our earlier SAXS data showing that the isolated Arc CT domain is fully monomeric [31].

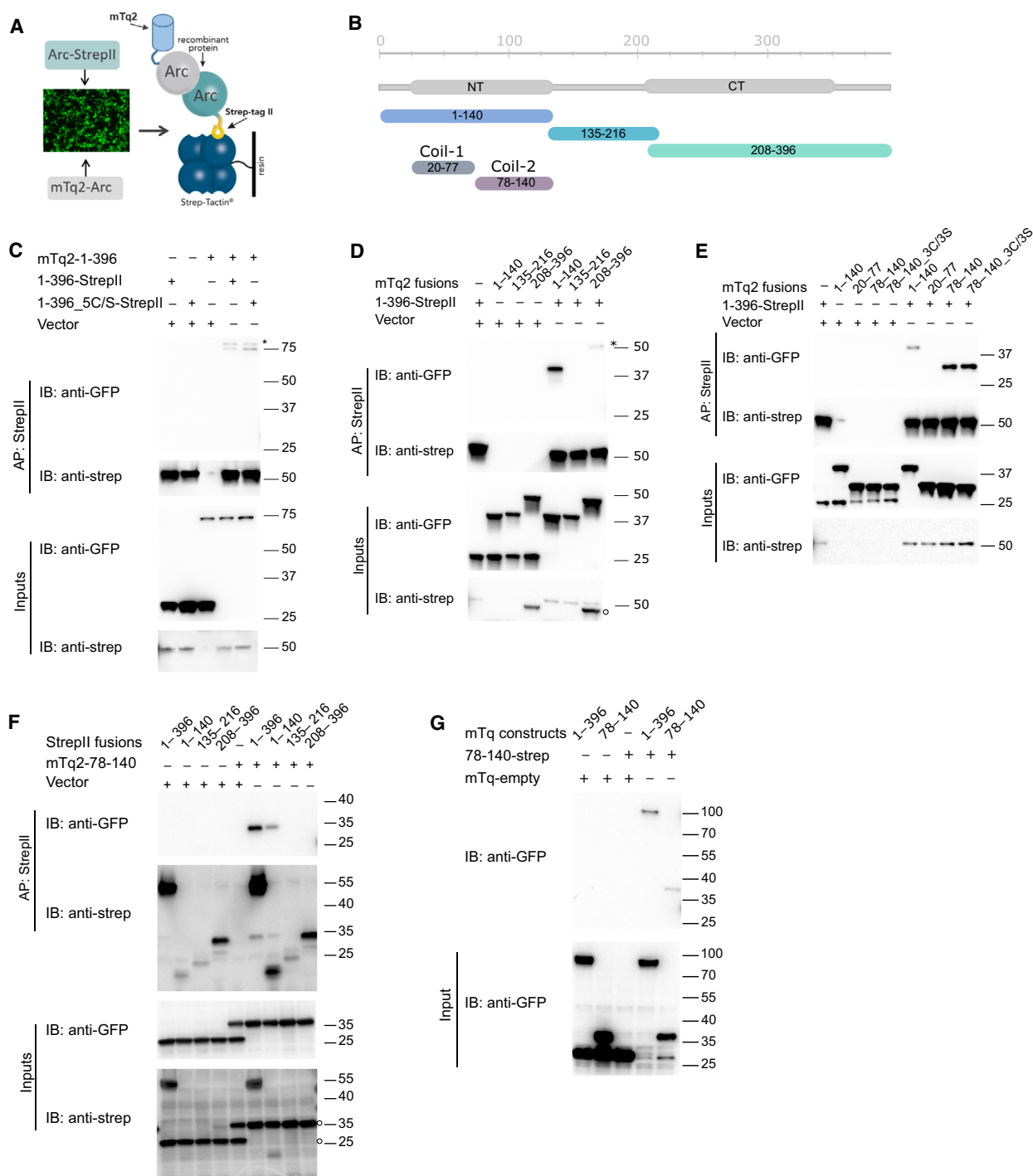
According to secondary structure predictions, the Arc NT domain has a coiled-coil region, with residues 20–77 and 78–140 corresponding to the first and second α -helix, respectively. Our previous structural analysis suggested an elongated, antiparallel coiled-coil structure of the NT domain [31]. We therefore examined copurification of full-length Arc with each of the NT domain coil regions. No interaction was observed with mTq2-fused Coil-1, whereas Coil-2 showed high-affinity binding (Fig. 1E). Similar binding to full-length Arc was obtained with a Cys to Ser mutant (3C/3S; residues 94, 96, and 98) of Coil-2, again ruling out formation of disulfide-linked oligomers (Fig. 1E). Coil-2 also copurified with the isolated Arc NT region, but not with the linker region or CT region (Fig. 1F). Furthermore, binding was observed between StrepII-tagged and mTq2-tagged Coil-2, demonstrating self-association of the Coil-2 region (Fig. 1G).

Identification of an oligomerization motif in Arc NT domain Coil-2

Next, we sought to delineate which residues within Coil-2 mediate Arc-Arc interaction. We first generated a series of deletion (Δ) mutants of Coil-2; 18-amino-acid stretches were removed, starting with every 9th consecutive residue, giving an overlap of 9 residues between the deleted regions (Fig. 2). Deletion mutants Δ 78–86, Δ 78–95, and Δ 114–131 did not bind full-length Arc (Fig. 3A). The Δ 78–86 and Δ 78–95 mutants were associated with decreased expression of the peptide, although the latter to a lesser extent. We then generated substitution (s) variants, in which non-overlapping stretches of seven amino acids were mutated to alanine (Fig. 2 and Fig. 3B). Except for s78–84A, which exhibited impaired expression, the substitution variants expressed at levels similar to WT control. Affinity purification analysis showed that all substitutions within the central region of Coil-2, from residue Gln99 to residue Trp126, inhibited binding of Coil-2 to full-length Arc (Fig. 3B). Importantly, oligomerization was similarly inhibited or abolished when mutations were introduced into full-length Arc (Fig. 3C). Most notably, alanine substitution of the sequence ${}_{113}\text{MHVWREV}_{119}$ (Arc^{s113–119A}) abolished binding to Arc-StrepII.

As a complementary approach, we mapped the NT domain Coil-2 interaction site using a peptide-tiling array of Arc 71–147. Each spot on the array displays a 21-residue peptide, with 7-residue overlap between sequences. The array was incubated with purified GST-fused Coil-2 and immunoblotted with anti-GST antibodies. Binding was observed with tiling peptides spanning Arc 99–126 (Fig. 3D, top panel). Pure GST did not bind to immobilized peptides (Fig. 3D, bottom panel). These *in vitro* binding results identify an oligomeric interface in Coil-2 and corroborate findings from affinity purification of tagged Arc from HEK cells.

Taken together, the results indicate that Arc region 99–126 in NT domain Coil-2 is necessary and sufficient for Arc oligomerization. We refer to this 28-amino-acid stretch as the oligomerization region, while the critical Arc 113–119 sequence is referred to as the oligomerization motif (Fig. 3E, top panel). The approximate position of the oligomerization motif in the context of the 3D model of the Arc monomer based on SAXS experiments [31] is shown in Fig. 3E (bottom panel). Sequence analysis of the oligomerization region predicts an amphipathic coil with hydrophobic residues packed on one side and polar residues on the other side (Fig. 3F).



Atomic-resolution crystal structure of oligomerization peptide identifies coiled-coil interface

The oligomerization region is predicted to adopt an α -helical conformation and self-associate. The α -helical

nature was confirmed by circular dichroism (CD) spectroscopy of a synthetic peptide (residues 99–132) containing the defined oligomerization region (99–126) and six additional C-terminal residues, which based on our analysis of substitution mutants may contribute to oligomerization (Fig. 4A). The peptide was

Fig. 1. Arc self-association is mediated by N-terminal domain Coil-2. (A) Model showing the principle behind affinity purification of Arc constructs coexpressed in a human embryonic kidney cell line (HEK293FT). (B) Schematic representation of Arc fragments used in the study. (C) mTurquoise2-fused (mTq2) full-length Arc was coexpressed with StrepII-tagged full-length Arc^{WT} or a five-site cysteine mutant. mTq2 (vector) was used as control. (D) StrepII-tagged full-length Arc was coexpressed with mTq2-fused Arc fragments (mTq2 fusions) as indicated by the numbers: 1–140, 135–216, and 208–396. (E) StrepII-tagged full-length Arc was coexpressed with mTq2-fused Arc fragments (mTq2 fusions: 1–140, 20–77, 78–140, and a cysteine-to-serine mutant of 78–140). (F) mTq2-fused Arc 78–140 was coexpressed with StrepII-tagged Arc as indicated by residue numbers (StrepII fusions: 1–140, 135–216, and 208–396). (G). StrepII-tagged Arc 78–140 was coexpressed with mTq2-fused full-length Arc or residues 78–140. Due to the small size of StrepII-tagged 78–140, we were not able to detect it by western blot analysis. (C–G) Cell lysates were incubated with Strep-Tactin Sepharose and the bound proteins eluted in sample buffer. Proteins were detected after SDS/PAGE and western blot analysis by anti-GFP and anti-Strep antibodies. Asterisks indicate unspecific bands with molecular weight too high compared with inputs. Open circles indicate remaining anti-GFP immunofluorescence from the first round of membrane probing. $N = 4$ per sample for western blots.

crystallized, and the structure was solved by experimental phasing using the single-wavelength anomalous dispersion (SAD) signal from the single sulfur atom in the peptide. The structure was refined at a resolution of 0.95 Å. A dimer of the peptide was present in the asymmetric unit, arranged into an antiparallel coiled-coil structure (Fig. 4B). This assembly directly suggests an antiparallel arrangement of interacting Arc NT domains in the context of Arc oligomers. The coiled-coil is formed through the tight interaction of hydrophobic patches on each long helix (Fig. 4C). The opposite face of the amphipathic helix carries several basic residues, causing high positive electrostatic charge, which could be important for binding to negatively charged membrane surfaces or RNA.

The 7-residue oligomerization motif (Arc 113–119) is located in the central part of the helices of the coiled-coil (Fig. 4D). The structure thus explains the effects of the 7-Ala mutation on Arc oligomerization. Based on the structure, targeted point mutations were made on Met113 and Trp116 (Fig. 4E), which both appear central to the coiled-coil and have a number of interactions in the assembly. As the dimerization interface of the Arc peptide is mainly formed by hydrophobic amino acids (Fig. 4C), we substituted Met113 and/or Trp116 with aspartic acid to block the interaction. Affinity purification analysis showed that mutation of Met113 and Trp116, singly or combined, made to the Coil-2 peptide or full-length protein, inhibited self-association with Arc^{WT} (Fig. 4F,G).

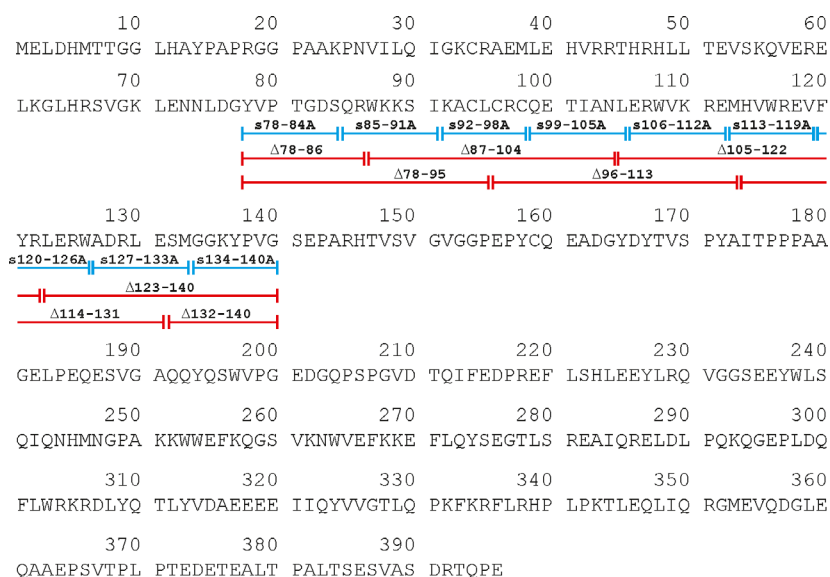


Fig. 2. Arc sequence depicting deletion mutants (red) and alanine substitution mutants (blue) within the NT domain Coil-2. Accession number and FASTA sequence retrieved from uniprot.org: Q63053 (ARC_RAT).

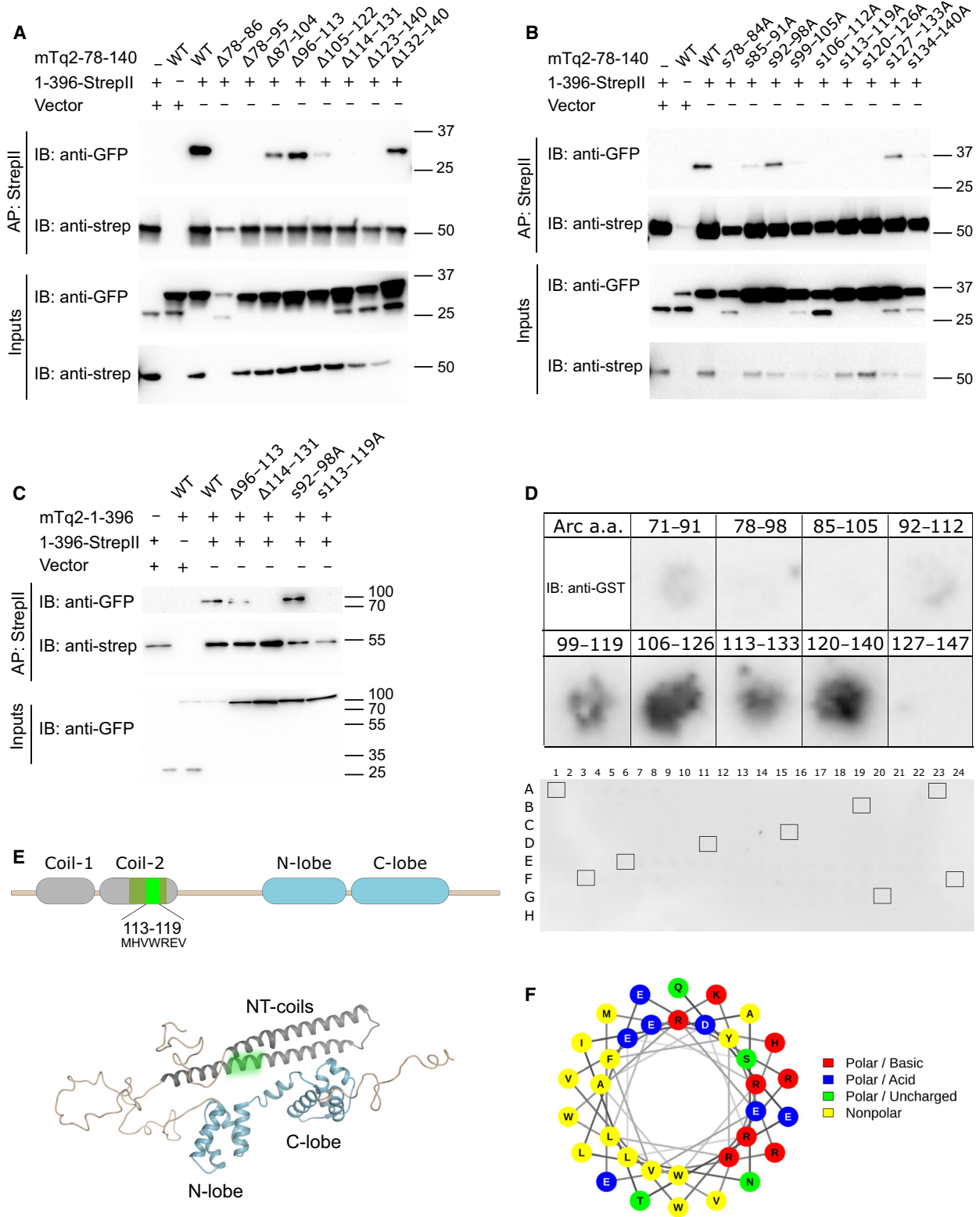


Fig. 3. Identification of an oligomerization interface in NT domain Coil-2. (A) StrepII-tagged full-length Arc was coexpressed with mTq2-fused Arc 78–140 wild-type or Arc 78–140 with 18 amino acids deleted as the numbers indicate. (B) StrepII-tagged full-length Arc was coexpressed with mTq2-fused Arc 78–140 wild-type or Arc 78–140 with 7-amino-acid alanine substitutions as indicated. (C) StrepII-tagged full-length Arc was coexpressed with mTq2-fused full-length Arc with either deletions or substitutions as indicated. In panels A–C, cell lysates were incubated with Strep-Tactin Sepharose and the bound proteins eluted in sample buffer. Proteins were detected after SDS/PAGE and western blot analysis by anti-GFP and anti-Strep antibodies. $N = 4$ per sample for western blots. (D) Upper panel. A peptide array consisting of 21-mer Arc peptides was incubated with GST-fused Arc 78–140. Probing with anti-GST revealed binding of Arc 78–140 to peptides spanning amino acids 99–126. (D) Lower panel. Probing with anti-GST did not show any unspecific interaction between Arc peptides and GST alone. Squares mark the Arc peptides shown in Fig. 3D as follows: A1-(71–91), A23-(78–98), B19-(85–105), C15-(92–112), D11-(99–119), E6-(106–126), F3-(113–133), F24-(120–140), and G20-(127–147). (E), Top panel. Position of the oligomerization region (residues 99–126, dark green) and oligomerization motif (residues 113–119, bright green) in NT domain Coil-2. (E), bottom panel. Approximate position of the oligomerization motif (bright green) in the full-length Arc 3D structure (SAXS hybrid model) [31]. (F) Helical wheel representation of the amino acids in oligomerization region showing the amphipathic nature of the peptide.

Fluorescence lifetime FRET imaging in hippocampal slices confirms self-association of Coil-2 mediated by the oligomerization motif

To assess Coil-2-mediated interactions in live neurons, we use fluorescence lifetime-based, Förster resonance energy transfer (FLIM-FRET) imaging in CA1 pyramidal cells of organotypic rat hippocampal slice cultures. Slices were transfected by gene gun with plasmids expressing Coil-2 fused to GFP (donor) and mCherry (acceptor) (Fig. 5A). In FLIM-FRET, a decrease in fluorescence lifetime of the donor, as measured by time-correlated single-photon counting, indicates increased protein–protein interaction. The fluorescence lifetime of WT GFP-NT-Coil-2 was equal to the positive control, an GFP-mCherry fusion that gives constitutive FRET (Fig. 5B), but significantly lower than the negative control (GFP-P2A-mCherry) in which the two fluorophores are separated by a self-cleaving peptide. Next, we examined the role of the oligomerization motif in mediating the interaction. When Coil-2 harboring the s113–119A mutation was used as the FRET acceptor, the interaction was significantly reduced compared with WT control (Fig. 5B). These live-imaging data show strong self-association of Coil-2 in hippocampal neurons and confirm a critical role for the oligomerization motif in the interaction. However, we also note that the FRET signal in the Coil-2 mutant did not reach the level of the negative control, indicating residual oligomerization.

In situ protein cross-linking reveals persistence of Arc dimer in oligomerization motif mutant

The findings from hippocampal slices suggested that the disruption of the oligomerization motif does not completely abolish Arc interactions, which contrasts with our findings from affinity purification of Arc expressed in

HEK cells. We therefore considered that cell lysis and homogenization might disrupt weak oligomeric interactions, as previously shown for α -synuclein [34]. To detect oligomeric species *in situ*, we examined Arc interactions in HEK cells treated with protein cross-linkers. Cells were transfected with constructs expressing mTq2-fused to Arc^{WT}, Arc^{s113–119A}, Arc^{s92–98A} (which does not affect self-association), or empty vector. In the main protocol used, cells were treated for 10 min with 100 μ M disuccinimidyl glutarate (DSG) before harvesting (Fig. 6). A strong Arc (and GFP) immunoreactive band was detected at 75 kDa, corresponding to monomeric mTq2-tagged Arc (Fig. 6A). In cross-linked preparations only, a strong Arc immunoreactive band was detected at approximately 180 kDa, likely corresponding to dimer, while a faint band at 300 kDa could correspond to a trimer or tetramer (Fig. 6A). The dimer was prominent for all constructs, with no difference in the dimer/monomer expression ratio, indicating that the s113–119A mutation does not disrupt dimer formation (Fig. 6B). However, the expression of the putative tetramer as a fraction of the dimer or monomer was significantly reduced in Arc^{s113–119A} relative to Arc^{s92–98A} and Arc^{WT} (Fig. 6C, D). These results reveal a prominent cellular expression of dimers in both Arc^{WT} and the oligomerization motif mutant and suggest a possible role for the oligomerization motif in assembly above the dimer stage.

The NT domain oligomerization motif is critical for formation of Arc capsids

A key question is whether the Arc oligomerization motif functions in capsid formation. In our first analysis of recombinant human Arc^{WT} by negative-stain transmission EM, we found irregular particles of ~ 30 nm diameter in samples that were prepared in HEPES buffer with high ionic strength [19]. Here, using PBS buffer in sample preparation, we found that

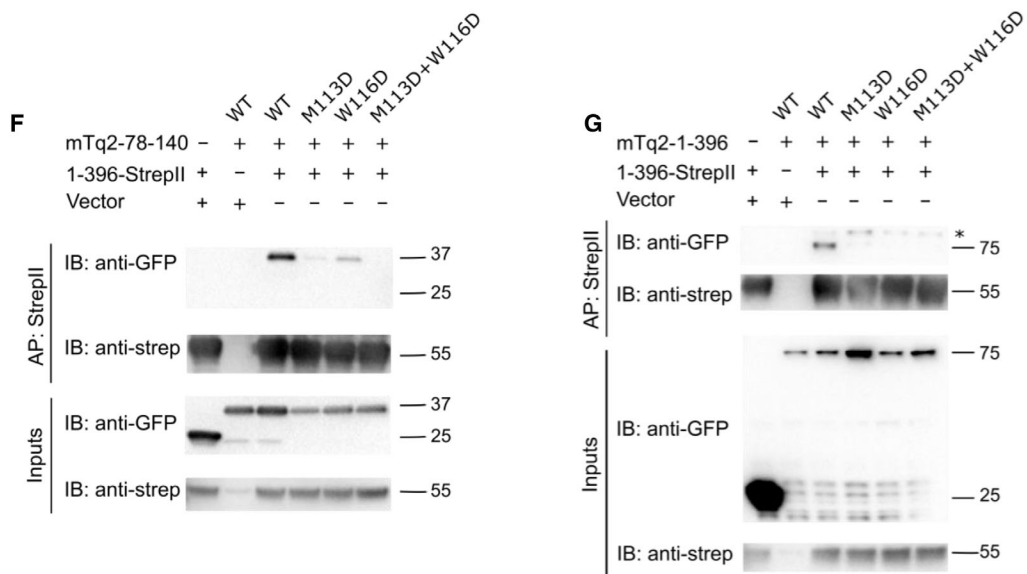
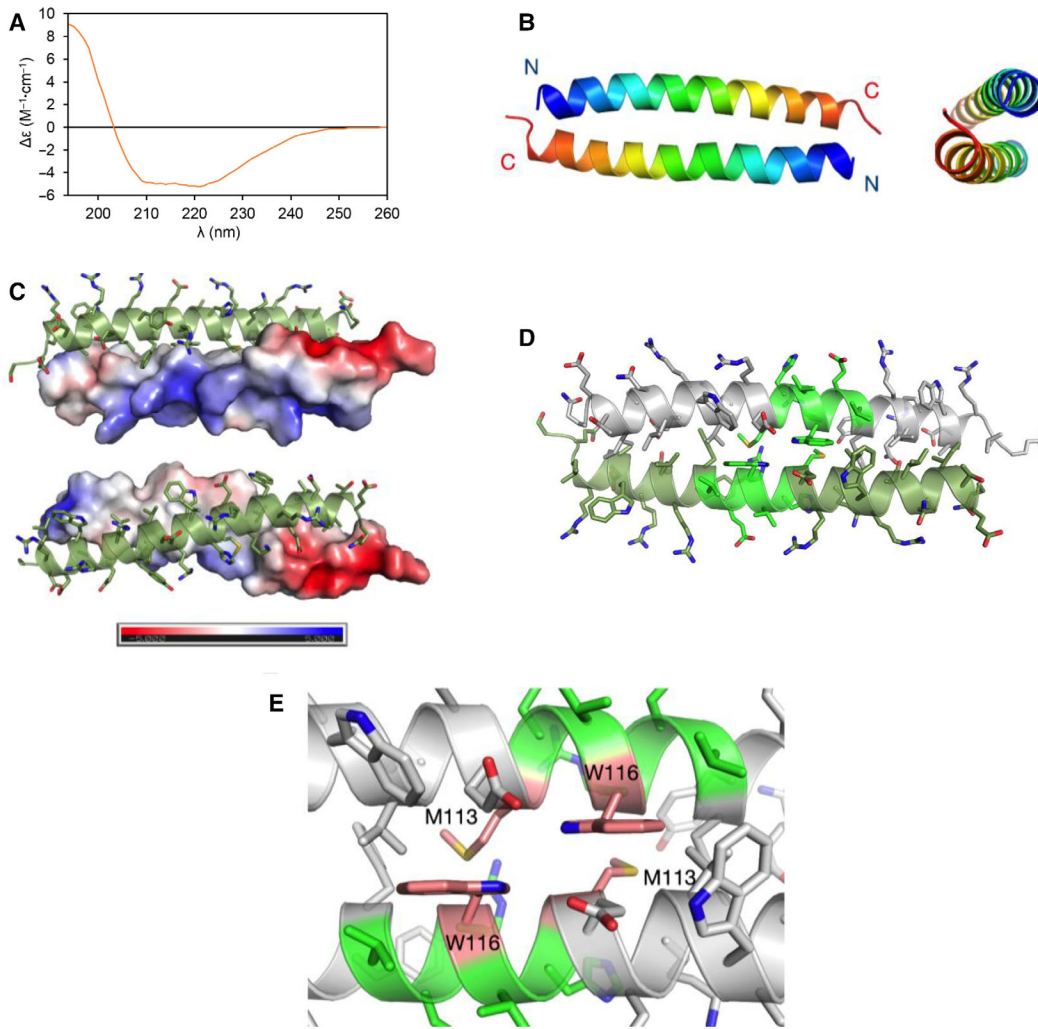


Fig. 4. Crystal structure of Arc oligomerization region peptide identifies a coiled-coil interaction surface and critical residues. (A) CD spectrum of Arc peptides 99–132 shows that the peptide adopts an α -helical conformation. (B) Crystal structure of the peptide shows assembly of the Arc antiparallel coiled-coil, colored from the N (blue) to the C (red) terminus. The view on the right is rotated by 90°. Panels (B–E) were prepared using PyMOL. (C) Electrostatic surface, calculated using APBS, of one monomer is shown to highlight the hydrophobic nature of the interface and the positive charge of the opposite face of the helix. (D) The 7-residue region 113–119 (light green) is central to the coiled-coil assembly. (E) The key residues Met113 and Trp116 (shown in orange) were shown to be important for Arc oligomerization through further structure-based mutagenesis (F, G). (F, G) Arc self-association is inhibited by aspartate substitution mutation Met113 (M113D) and Trp116 (W116D) in the oligomerization motif. Affinity purification analysis was performed in HEK cell lysates. In panel F, StrepII-tagged full-length Arc was coexpressed with mTq2-fused Arc 78–140 wild-type or Arc 78–140 with indicated mutations. In panel G, StrepII-tagged full-length Arc was coexpressed with mTq2-fused full-length Arc wild-type or full-length Arc with indicated mutations. Lysates were incubated with Strep-Tactin Sepharose and the bound proteins eluted in sample buffer. Proteins were detected after SDS/PAGE and western blot analysis by anti-GFP and anti-Strep antibodies. The asterisk indicates an unspecific band of molecular weight higher than input. $N = 4$ per sample for western blots.

human Arc^{WT} formed rounded, virus-like capsids (Fig. 7A,B) as seen with both negative-stain and cryo-EM, similar in size and shape to those reported for recombinant rat and *Drosophila* Arc [21,24,25,29]. The majority of capsids had a diameter of ~ 30 nm, although there was heterogeneity in size.

Next, we used dynamic light scattering (DLS) to estimate the size of purified Arc^{WT} and Arc^{S113-119A} (Fig. 7C). The main population of Arc^{WT} ($97.3 \pm 2.7\%$ of the intensity) had a mean diameter of 31.5 ± 1.2 nm, corresponding well to the capsid diameter seen by EM. In contrast, the main population of Arc^{S113-119A} ($95.7 \pm 2.9\%$ of the intensity) had a mean diameter of 13.1 ± 1.5 nm. Both proteins display one population by volume (Fig. 7C, inset) with 40–45% polydispersity. Further analysis by size-exclusion chromatography–multi-angle light scattering (SEC-MALS) showed elution of Arc^{S113-119A} as a single peak with a mass of 106 kDa, corresponding to a homodimer (Fig. 7D), and together with the DLS data, we confirm that this mutant does not form higher-order oligomers. As expected, Arc^{WT} eluted in the void, as was also recently reported [21].

Importantly, negative-stain transmission EM analysis of the mutant revealed a homogeneous population of small elongated particles (Fig. 7E), with no sign of capsid-like structures. We performed single-particle 3D EM reconstruction of 55,057 automatically selected particles from the Arc^{S113-119A} sample. The structure obtained, with no symmetry imposition, has a rhomboid, symmetrical shape (Fig. 7F, left). The size ($\sim 130 \times 85$ Å) and the apparent symmetry suggest that the particles are formed by a dimer of the Arc^{S113-119A} mutant. A subsequent refinement with C2 symmetry rendered a similar volume (Fig. 7F, right), and docking of the SAXS-based model of monomeric Arc [31] fits with the volume of a dimer, in two different orientations (Fig. 7G; models A (left) and B (right)). The best fitting is obtained

with model A, in which the alanine substitution in Arc^{S113-119A} would disrupt the presumed interactions between dimers in virus-like particles, while the NT-NT intradimeric interactions are maintained. In model B, the NT coils are more exposed, possibly favoring the NT-mediated interactions, while the dimer interface is mediated by CT-CT interactions. Model B better illustrates the possibilities for domain swapping (see below; Fig. 8). It must be taken into consideration that there are alternative ways of fitting a dimer into the envelope and that this is a stable and symmetric dimer. Despite providing valuable structural determinants on capsid formation, the dimer may have undergone some restructuring as compared with a dimer integrated in the virus-like capsid, as observed for mutant CA dimers [35]. In any case, the exact details need to be resolved with higher-resolution methods.

Small-angle X-ray scattering analysis of the mutant independently gave a volume corresponding to a dimer closely resembling the 3D EM reconstruction, with a more elongated shape (Fig. 8). SAXS is sensitive to disordered regions and such a difference is thus expected, showing the presence of flexible regions at the ends of the dimer. An elongated dimer shape was also obtained when Arc^{S113-119A} was N-terminally fused to MBP, and the external positions of MBP in the SAXS structure indicate an outward orientation of the NT domain in the dimer (Fig. 8). We conclude that the NT domain oligomerization motif supports Arc oligomerization above the dimer stage and is required for capsid formation.

Single-molecule imaging of Arc oligomeric state: critical role of NT domain coil motif in mRNA-induced oligomerization

In order to rigorously quantify the oligomeric state of Arc, we employed single-molecule total internal

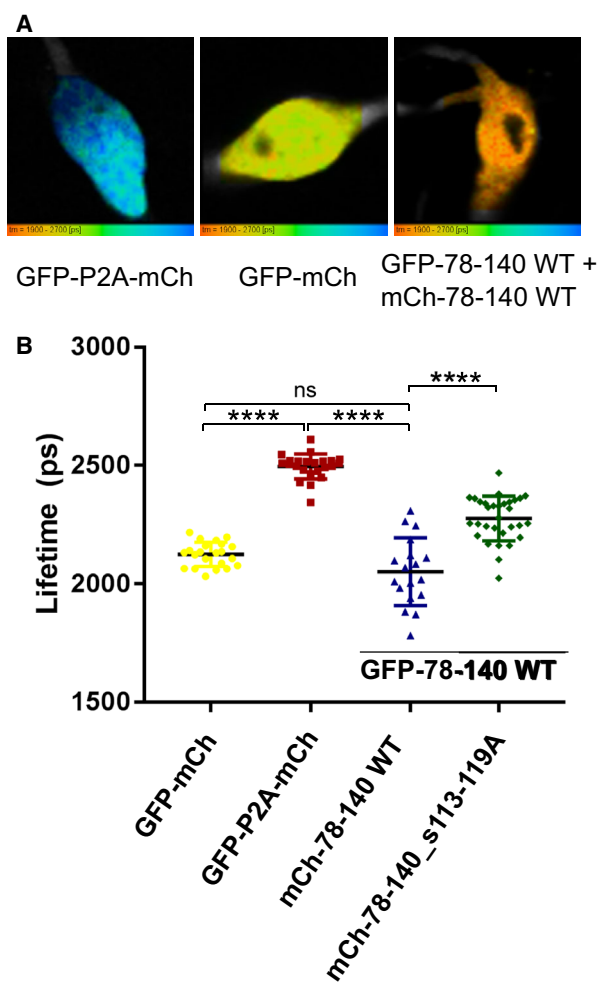


Fig. 5. Fluorescence lifetime FRET imaging of Coil-2 self-association in CA1 pyramidal cells of organotypic rat hippocampal slice cultures. (A) Representative FLIM-FRET images of CA1 pyramidal neuron somata-expressing Arc Coil-2 (78-140) fused to GFP donor and mCherry (mCh) acceptor, negative control (GFP-P2A-mCh), or positive control (GFP-mCh). Pseudocolor scale of fluorescence lifetime measurements from 1900 to 2700 ps. (B) Lifetime distribution of analyzed cells. Replacement of mCh-78-140 (WT) with 78-140 harboring the s113-119A mutation inhibited the interaction. Lines indicate mean and standard deviations. One-way ANOVA between groups with Tukey's multiple comparisons post hoc correction. **** $P < 0.0001$. $n = 22, 23, 18,$ and 31 , for GFP-mCh, GFP-P2A-mCh, Arc WT, and Arc 113-119, respectively.

reflection fluorescence (smTIRF) microscopy. For these experiments, we used recombinant rat Arc with an N-terminal SNAP tag and a C-terminal AviTag. Purified Arc was labeled with an Alexa Fluor 488 SNAP substrate, C-terminally biotinylated, and affixed onto glass cover slides through streptavidin binding (Fig. 9A). The size of each Arc oligomer was determined by photobleaching, where the number of

photobleaching steps corresponds to the number of dye molecules, and therefore the number of Arc monomers in each oligomer (Fig. 9 and Fig. 10).

Arc samples were imaged using smTIRF, where each fluorescent spot corresponds to one oligomeric complex (Figs 9A and 10). Spots with clearly identified steps of greater than 2 arbitrary units (A.U.) over 5 frames were used to calculate the step size for each experiment (see examples in Fig. 10). The number of photobleaching steps per spot was then determined by dividing the total intensity by the calculated step size (Fig. 9B). The initial intensity is proportional to the number of fluorophores per spot (Fig. 9C,F). From these initial intensities, we calculated the number of photobleaching steps, which suggest that lower-order Arc oligomers of fewer than 10 molecules exist predominantly as dimeric and trimeric species. In Tris buffer (pH 7.5), Arc^{WT} had a median step size of $2.61 (\pm 1.42 \text{ S.D.}, 0.068 \text{ S.E.M.})$. Similarly, the Arc^{s113-119A} mutant also showed the presence of lower-order oligomeric species with an average step size of $2.64 (\pm 0.89 \text{ SD}, 0.038 \text{ SEM})$. These data show that Arc is mainly dimeric/trimeric in Tris buffer.

Arc capsid formation was shown to be facilitated by the addition of EGFP mRNA [25]. However, the mechanism of the EGFP mRNA effect is unknown. Interestingly, studies of Gag lattice assembly show that nonspecific binding to RNA promotes Gag multimerization [22,36]. The Arc NT domain is highly basic, and the amphipathic coil presents a surface of positive charge that may promote RNA interactions. We therefore speculated that Arc oligomerization is facilitated by mRNA in a manner dependent on the oligomerization motif. To address this question, we added exogenous EGFP mRNA to purified Arc before attaching it to coverslips. When EGFP mRNA was added to purified Arc^{WT}, the median oligomer size increased to 4.1 ($P < 0.0001$), whereas when EGFP was added to Arc^{s113-119A} mutant, there was no shift in oligomer size (Fig. 9D). Under physiological conditions in neurons, Arc protein interaction with Arc RNA might impact oligomerization. We therefore also examined the effect of purified Arc mRNA. Arc mRNA addition to Arc^{WT} and Arc^{s113-119A} mutant protein caused the median oligomer size to increase in both samples (4.7, $P < 0.0001$, and 6.1, $P < 0.0001$, respectively) (Fig. 9G). Arc mRNA is 1467 nt, and EGFP mRNA is 720 nt. The longer Arc mRNA appears to facilitate lower-order oligomers that are larger than dimers for both Arc^{s113-119A} and Arc^{WT} (96% of molecules in both samples). In contrast, EGFP mRNA addition results in a larger proportion of smaller species with

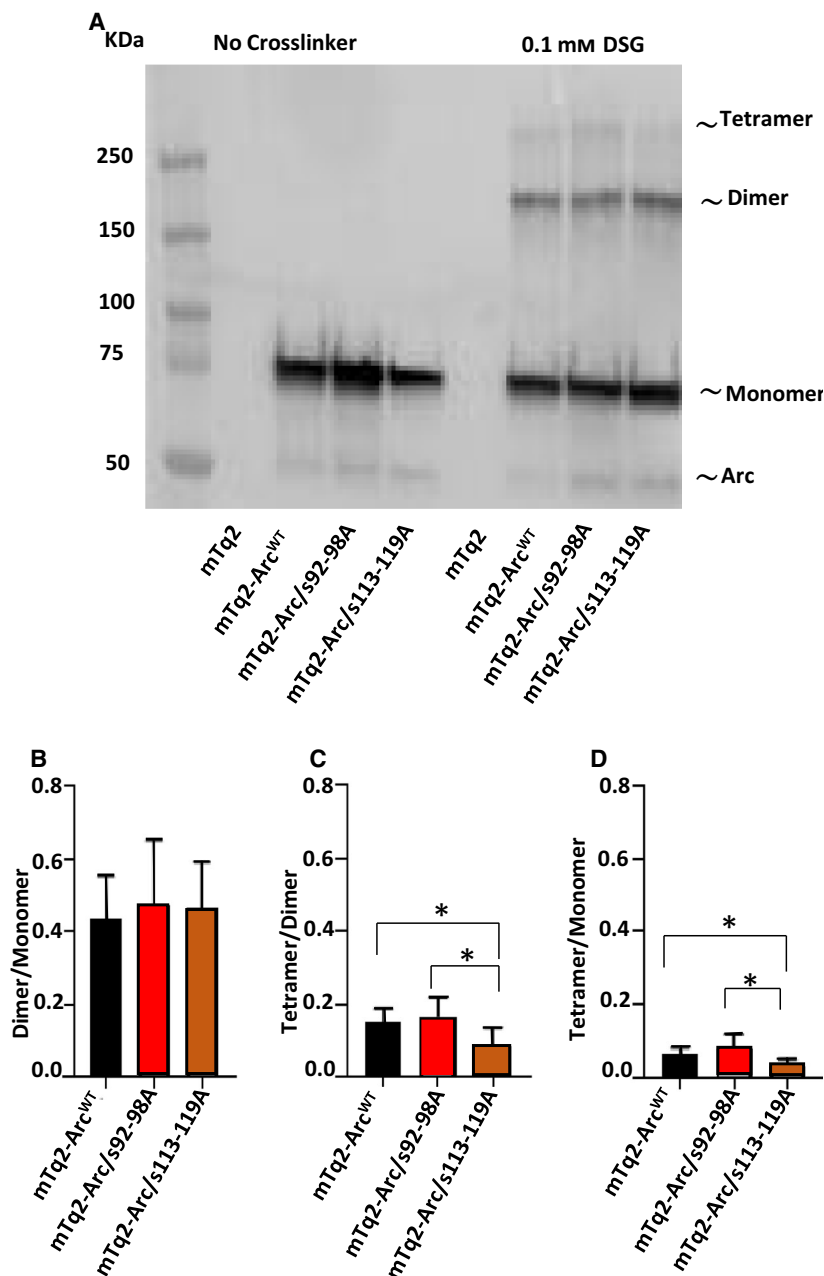


Fig. 6. In situ protein cross-linking reveals a prominent Arc dimer but inhibition of tetramer formation in the oligomerization motif mutant. HEK293FT cells were transfected with Arc^{WT}, Arc^{s92-98A}, or Arc^{s113-119A}, all tagged at the N terminus with mTurquoise2. For cross-linking, cells were treated with disuccinimidyl glutarate (DSG) dissolved in DMSO to a final concentration of 0.1 mM for 10 min. (A) Arc immunoreactive bands were detected at ~ 75 kDa, 180 kDa, and 300 kDa corresponding to mTq2-tagged Arc monomer, dimer, and a putative tetramer. A band at 50 kDa is probably an Arc cleavage product. Oligomers were detected only in cross-linked samples. Similar results were obtained with paraformaldehyde cross-linking (not shown). (B) Ratio of Arc monomer/dimer expression. (C) Ratio of tetramer/dimer expression. (D) Ratio of tetramer/monomer expression. Values in bar graphs are mean + S.E.M. N = 6. One-way ANOVA with Bonferroni multiple comparison was used for statistical analysis **P* < 0.01.

1–3 subunits per complex: 29% for Arc^{WT} and 58% for Arc^{s113-119A}. The results show that exogenous mRNA facilitates lower-order Arc oligomerization, and this response depends on the oligomerization motif and the length of mRNA. The lack of monomers or dimers in the Arc mRNA-treated samples suggests that these species more efficiently oligomerize in response to Arc mRNA.

We separately analyzed discrete brighter fluorescent spots with and without addition of both types of mRNA. These brighter spots correspond to higher-

order oligomeric species. It is not reliable to determine the number of steps in the higher-order oligomers due to the large number of clustered fluorophores. This results in limited discrete steps, which confounds our analysis. However, if we assume that the step size is the same (given that the fluorophore is the same) we estimate the size of the higher-order oligomers is between 30 and 170 monomers of Arc per complex. These brighter spots were extremely uniform (Fig. 10). Arc aggregation on the slides was sometimes detected, and these very bright amorphous regions were not

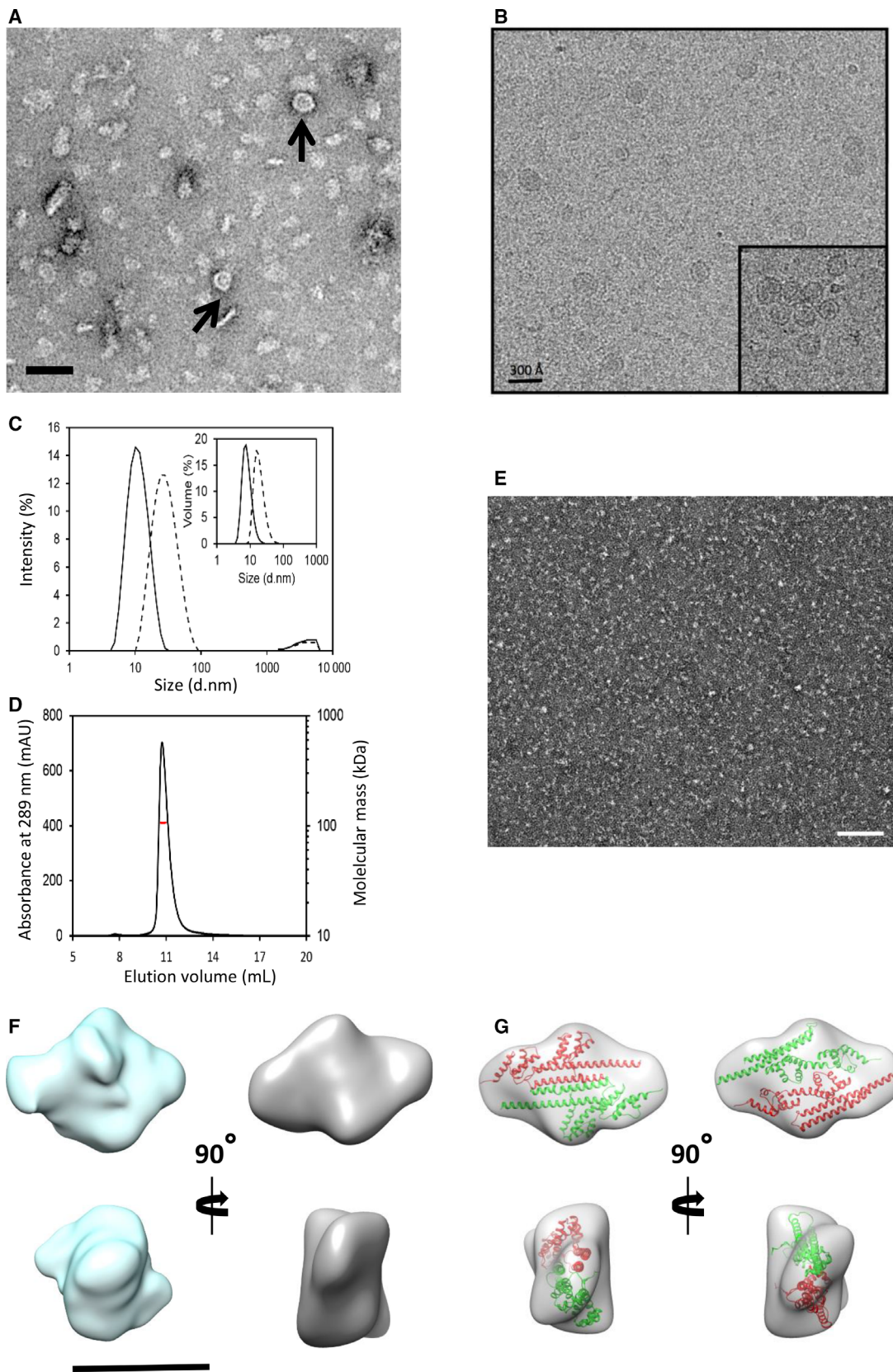


Fig. 7. The Arc s113–119A oligomerization motif mutant forms dimers but not virus-like capsids. (A) Electron microscopy image of negatively stained Arc preparation. The sample shows particles of different sizes, aggregates, but also spherical capsid-like structures of ~ 300 Å diameter (arrows). In most cases, capsids contain an electron-dense substance. Scale bar, 600 Å. (B) Cryo-electron microscopy image of Arc. Some capsid-like structures of similar size to those obtained in A are observed. The inset shows a homogeneous group of several of these structures. Scale bar, 300 Å. (C) DLS analysis with size-estimation of purified Arc^{WT} (dashed line) and Arc^{s113–119A} (solid line) based on intensity and volume (inset) size distribution. (D) SEC-MALS analysis of the Arc^{s113–119A} mutant. (E) Electron microscopy image of negative-stained Arc^{s113–119A} mutant (right). Bar indicates 50 nm. (F) Two orthogonal views of the 3D reconstruction of the Arc^{s113–119A} mutant without symmetry imposition (left) and with C2 symmetry imposed (right). (G) Docking, using the same two orthogonal views of the C2 symmetrized 3D reconstruction, of two copies (red and green) of the atomic structures of the predicted N-terminal coiled-coil domain (4x3i.pdb; [31]) and the two-lobe structure of the C-terminal domain (6GSE, [21]). The docking shows that two Arc monomers can fit in the reconstructed volume but does not necessarily represent the actual structure of the dimer. Because of the low resolution of the 3D reconstruction, two general dockings are possible: left, with the N-terminal, coiled-coil domains of the two subunits at the center of the structure; right, with the two C-terminal lobes at the center of the structure. Visualization of the 3D models and docking of the atomic structures into EM volumes was performed manually using UCSF Chimera. Images in panels A, B, and E are representative images, each based on two independent protein preparations, with 10 replicates for each preparation.

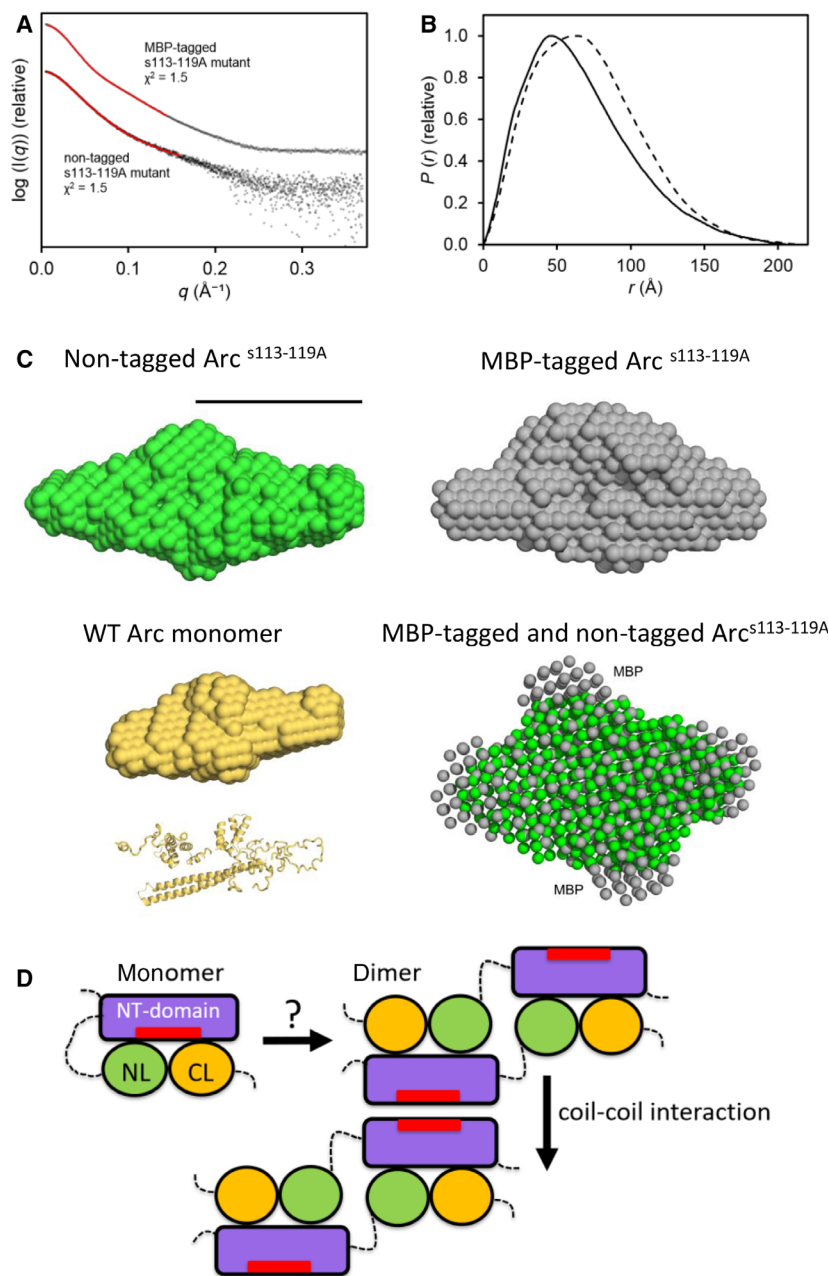


Fig. 8. SAXS analysis of Arc s113–119A mutant with and without N-terminal MBP tag. (A) SAXS scattering profiles for purified recombinant rat Arc s113–119A mutant protein, MBP-tagged and nontagged, with fits of generated *ab initio* dummy atom models in red. (B) SAXS distance distribution functions for purified recombinant rat Arc s113–119A mutant protein, MBP-tagged (dashed) and nontagged (solid). (C) Dummy atom models of purified recombinant rat Arc s113–119A mutant protein, MBP-tagged (gray) and nontagged (green), and purified recombinant human Arc wild-type monomeric protein (yellow). Below the yellow DAMMIN model is a CORAL hybrid model of purified recombinant human Arc wild-type monomeric protein. Yellow models come from reference (12). Bottom right: the SAXS-based average *ab initio* models of the Arc dimer with and without the MBP tag indicate the position of the MBP moiety in the dimer, and hence, the position of the Arc N terminus. The result shows that the NT domain is on the outside of the Arc dimer. (D) A domain-swapped model for the dimer fits the currently available data. A red bar indicates the predicted location of the oligomerization region.

analyzed. In the samples where EGFP mRNA was added, the majority (84%) of the higher-order oligomers were in the range of ~40–70 subunits per complex (Fig. 9E). When Arc mRNA was added, nearly all (99.5%) of the higher-order oligomers were between 70 and 100 subunits per complex (Fig. 9H). In the absence of mRNA, there were very few classified higher-order oligomers for both Arc^{WT} (mean 8.5) and Arc^{s113–119A} (mean 1.5) (Fig. 9E,H). However, when EGFP or Arc mRNA was added to Arc^{WT}, there was a 19-fold and 30-fold increase, respectively, in the number of higher-order oligomers compared with Arc^{WT} alone (Fig. 9E, H). In striking contrast, the number of higher-order oligomers in Arc^{s113–119A} samples treated with EGFP mRNA or Arc mRNA was 0 and 6, respectively. These findings show that higher-order oligomerization of Arc is greatly enhanced by exogenous mRNA (both EGFP and Arc) through a mechanism that requires the NT domain oligomerization motif.

Mutation of the Arc oligomerization region impairs transferrin endocytosis

Arc is an adaptor protein for clathrin-mediated endocytosis and facilitates cellular uptake of transferrin [4]. Upstream of the oligomerization region, Coil-2 harbors an endophilin-binding site determinant (residues 89–100) involved in endocytosis [4]. This short stretch also contains a cysteine cluster, ₉₄CLCRC₉₈, involved in palmitoylation and membrane targeting of Arc [32]. Mutations to this part of Coil-2 do not affect self-association in the affinity purification assay, as shown in Fig. 3. Here, we asked whether disruption of the oligomerization region affects endocytosis, as assessed by uptake of Alexa Fluor 647-conjugated transferrin in HEK cells (Fig. 11A). As expected, the expression of Arc^{WT} enhanced transferrin uptake relative to empty vector control (Fig. 11B). Expression of the endophilin-binding site mutant, Arc^{s92–98A}, failed to increase transferrin uptake (Fig. 11B), although the protein successfully forms oligomers (Fig. 3B,C). Notably, the oligomerization-deficient Arc mutants (Δ 114–131 and s113–119A) failed to facilitate transferrin uptake (Fig. 11B). As levels of monomer and dimer expression did not differ between Arc^{s113–119A}, Arc^{s92–98A}, and Arc^{WT}, these results support a role for oligomerization above the dimer stage in promoting endocytic activity, which also requires the endophilin-binding site.

Discussion

Arc is both a hub protein for intracellular signal transduction in mammalian brain and capable of forming

retrovirus-like capsids for transmission of mRNA in extracellular vesicles. Here, we found that NT domain Coil-2 harbors a critical molecular determinant of Arc self-association, mRNA interaction, and capsid formation.

The ancient retroviral origin of Arc invites a comparison with the extensively studied domains of retroviral Gag. The Gag MA, CA, and nucleocapsid (NC) domains each play distinct and crucial roles in the formation of the immature virion [22,30]. The core lattice of the retroviral capsid is formed by dimerization of CA domains which assemble into a hexameric core, and the isolated recombinant CA self-associates *in vitro* [37,38]. The situation in mammalian Arc is surprisingly different. In striking contrast to Gag CA, the homologous Arc CT domain and its separated N and C lobes are fully monomeric (present study and [21,31,39]). The recombinant Arc C-terminal region also fails to form regular capsids suggesting that full-length protein is needed for assembly [25]. Here, we identified a 28-residue oligomerization region in NT domain Coil-2 that undergoes self-association. Within this region, we discovered a 7-residue motif, ₁₁₃MHVWRE_{V119}, critical for oligomerization of full-length Arc and capsid formation. The impact of the motif on capsid formation and interactions with mRNA is based on the use of 7-alanine substitutions. Crystal structure analysis of the isolated oligomerization region revealed Met113 and Trp116 as critical residues at the interface between helices of an antiparallel coiled-coil, and point mutations to Asp in either residue inhibited self-association of full-length Arc.

The Gag NC domain has a dual function in binding viral and host RNA. Recognition of viral genomic RNA sequences is mediated by trans-acting zinc finger motifs [22,40]. In addition, a patch of basic residues at the NC N-terminus mediates nonspecific binding to host RNA [22,41], which is proposed to function as a scaffold for Gag-Gag interactions [36,42–47]. Mammalian Arc does not have amino acid sequence similarity to Gag NC and lacks a zinc finger. However, similarly to the NC domain, the Arc oligomerization region (99–126) has positively charged patches that may interact with polyanionic RNA. The fact that both Arc mRNA and EGFP mRNA strongly enhanced oligomerization indicates an electrostatic interaction rather than RNA sequence-specific binding to the protein. Notably, previous studies showed that the replacement of the NC domain with a leucine zipper coiled-coil is sufficient to reinstate nucleic acid-induced Gag multimerization [48,49]. Thus, the mammalian Arc NT domain resembles Gag NC in mediating RNA-induced multimerization.

The Arc NT domain is physicochemically similar to retroviral MA. The MA domain is critical for targeting of Gag to the plasma membrane, which involves a patch of basic residues (the highly basic region), MA myristoylation, and binding of host tRNA [22,50]. Similarly, Arc interaction with phospholipid membrane is mediated by electrostatic interactions and palmitoylation of the NT domain. The palmitoylation occurs within a putative endophilin-binding site [31,32]. Here, we found that mutation of the region containing the palmitoylation sites inhibited endocytosis without affecting Arc self-association. However, mutations that blocked self-association also inhibited endocytosis. This suggests that Arc self-association might facilitate endocytic activity of Arc, which is in line with recent observations [18,39]. Taken together, the evidence suggests that the uniquely mammalian NT domain is critical for membrane binding, self-association, and RNA interactions that promote oligomerization. In this respect, the Arc NT domain shares functional properties with Gag CA and NC, as well as the MA domain.

Drosophila Arc proteins, dArc1 and dArc2, have CA-like domains that form capsids [9,24,28,29]. dArc1, but not dArc2, has a zinc finger at its C-terminus homologous to the Gag NC zinc fingers. Only dArc1 capsids contain Arc mRNA, implying a role for the zinc finger in binding dArc1 mRNA [24]. Recently, single-particle cryo-EM was used to determine structures of dArc capsids, revealing that both homologs assemble into icosahedral capsids in which the capsid shells are formed by 240 copies of dArc CA [29]. Upstream of CA, there is an N-terminal stretch of 41 and 28 residues in dArc1 and dArc2, respectively, predicted to form amphipathic α -helices. In the cryo-EM structure, some of these segments appear to form spikes that extend outward from the capsid shell, whereas others protrude inward. The spikes effectively occlude openings in the shell, and it has been suggested they could be involved in membrane interactions and regulation of access to the capsid interior [29].

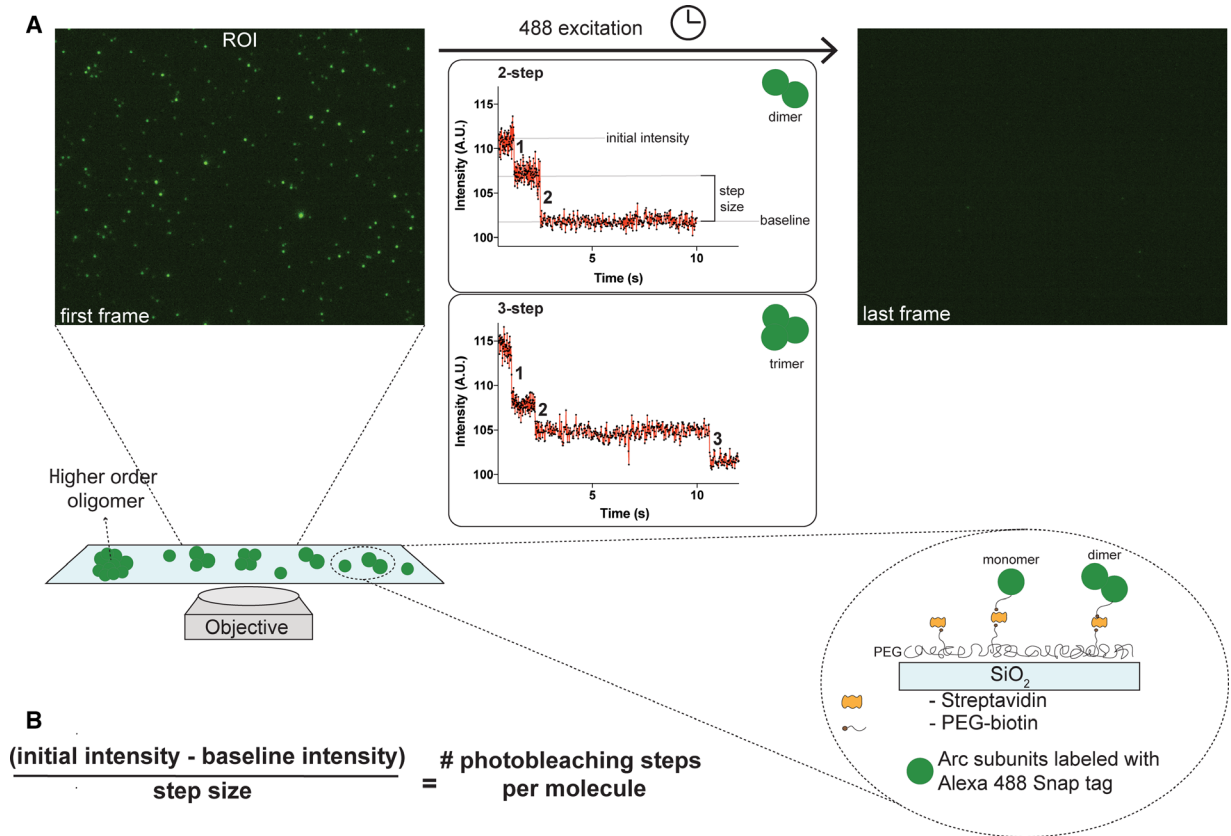
The structure of mammalian Arc capsids is unknown. We obtained a mean capsid diameter of 30 nm for human Arc, in agreement with rat Arc capsids, while dArc capsids are 37 nm in diameter [21,24,25,29]. Our measurements of the capsid layer suggest a thickness of ~ 3 nm. By calculating the volume of the capsid layer ($6.9 \times 10^6 \text{ \AA}^3$) and taking into account the average density of a globular protein (0.85 Da/\AA^3) and the molecular mass of human Arc (45 kDa), this gives an average of 130 copies of the protein per capsid. This size fits with the smTIRF analysis indicating that

the majority of higher-order oligomers contain between 40 and 100 units with some larger species up to 170 units. A lower number of protein copies in the human Arc capsid compared with fly Arc agrees well with the smaller size of the human Arc capsid and the larger size of the protein, due to the larger 206 residue N-terminal and linker region in human Arc.

Purified MBP-tagged and untagged Arc^{S113-119A} formed a homogenous stable dimer population, and single-molecule imaging of the tethered protein showed an average size between dimer and trimer. No capsids and almost no higher-order oligomers were detected for the mutant. Tagging of proteins may influence the oligomerization. However, we observed overall concordance between the methods. Both SAXS and single-particle EM reconstruction of Arc^{S113-119A} fit well with the presence of two full-length Arc monomers [31] inside the elongated volume (Fig. 7 and Fig. 8). SAXS analysis of MBP-fused Arc^{S113-119A} further shows N-termini on the outside of the dimer, consistent with CT domain involvement at the dimer interface. In the full-length Arc monomer, the NT and CT domains interact, stabilizing the flexible linker region [31]. In the dimer, a domain swap could take place, allowing NT-CT domain interactions to occur between monomers (model in Fig. 8). We propose that the N-terminal oligomerization motif is accessible in the dimer, and disruption of the motif abolishes mRNA-induced facilitation of higher-order oligomers.

Although the isolated Arc CT domain is monomeric in solution [21,31], it has dimerization motifs homologous to retroviral CA that could play a role in the context of the full-length protein. A recent dynamic light scattering analysis showed that mutation of predicted dimerization sites in the CT domain impaired oligomerization of full-length protein above the tetramer stage [39]. As the oligomerization region in Coil-2 is the only Arc region known to self-associate, it will be important to determine whether the NT domain enables CT-CT domain interactions. The mechanism of Arc dimer formation is still unknown, as it does not depend on the identified oligomerization determinants.

Studies of synaptic plasticity in mammalian brain have demonstrated a tight spatial-temporal coupling between Arc mRNA and protein expression [1,51-53]. The present *in vitro* work employing the purified Arc mRNA coding region and recombinant protein implies a possible physiological role for the mRNA at different stages of oligomerization. While the disruption of the oligomerization motif inhibited mRNA-induced higher-order oligomerization, lower-order oligomerization was facilitated in both mutant and wild-type. Efficient assembly of lower-order oligomers is also



B

$$\frac{(\text{initial intensity} - \text{baseline intensity})}{\text{step size}} = \# \text{ photobleaching steps per molecule}$$

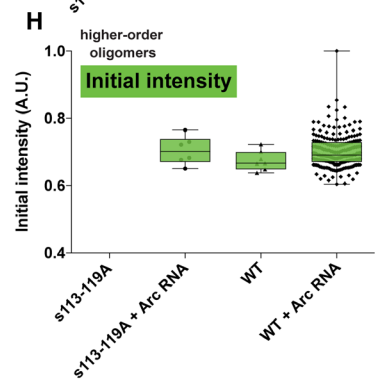
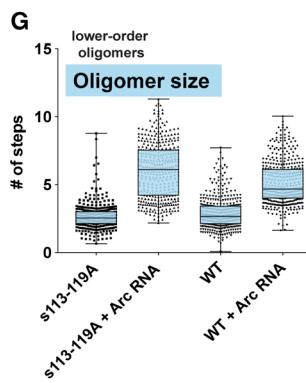
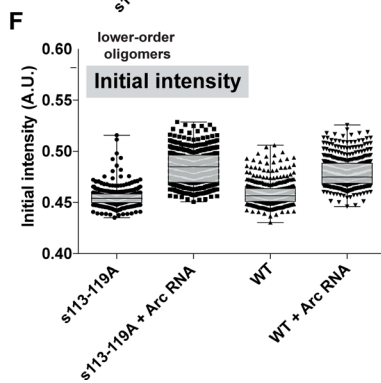
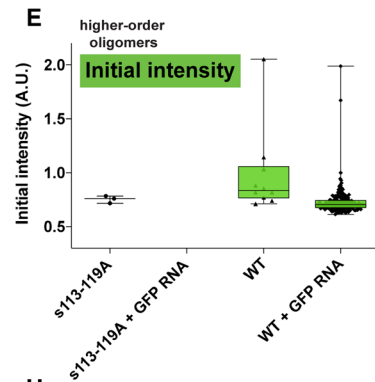
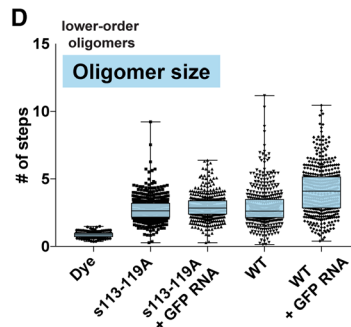
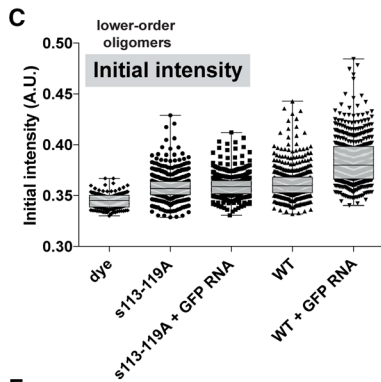


Fig. 9. Single-molecule TIRF analysis of Arc reveals critical role of oligomerization motif in RNA-induced higher-order oligomerization. (A) Flowchart of the photobleaching experiment using single-molecule TIRF microscopy. Biotinylated Arc is affixed to glass cover slides using a PEG-biotin/streptavidin linkage, as shown. A region of interest (ROI) is exposed to constant 488 nm excitation, causing molecules to photobleach over time. Examples of the first and last frames from a photobleaching video are shown. If the single molecule is an Arc dimer, 2 discrete photobleaching steps are observed. Examples of 2-step and 3-step photobleaching are shown. (B) Equation used to calculate number of photobleaching steps per molecule. (C) We compared the initial intensity (first frame of ROI) of single molecules of several samples and conditions (see X-axis label). Molecules with an initial intensity less than ~160 A.U. were considered lower-order oligomers. Box and whisker plots show the 10th-90th percentile data points for clarity. (D) After calculating the step size from each experiment (see A), the initial intensity was converted to number of steps (see B). The number of photobleaching steps for the lower-order oligomers is plotted. The number of steps correlates to the size of oligomer (i.e., 4 photobleaching steps indicates a tetrameric complex). When comparing EGFP mRNA and Arc^{WT} ($n = 436$ without EGFP mRNA, $n = 445$ with Arc mRNA), the median oligomer size increased to 4.1 (± 1.77 S.D., 0.084 S.E.M.), $t(437) = -11.1607$, $P < 0.0001$, whereas EGFP mRNA addition to Arc^{s113-119A} mutant ($n = 448$ without EGFP mRNA, $n = 431$ with Arc mRNA), there was no shift in oligomer size, $t(409) = -4.6394$, $P < 0.0001$. No shift was observed when comparing Arc^{WT} to Arc^{s113-119A}, $t(437) = 3.2998$, $P < 0.01$. (E) For the same samples as in B, we separately analyzed molecules brighter than 160 A. U., which were considered higher-order oligomers. The initial intensity of all molecules that qualified is plotted. (F–H) Same as (C–E) but with Arc mRNA. Arc mRNA addition to purified Arc^{WT} ($n = 389$ without Arc mRNA, $n = 422$ with Arc mRNA) and Arc^{s113-119A} mutant ($n = 391$ without Arc mRNA, $n = 379$ with Arc mRNA) caused the median step size to increase in both samples (4.7 (± 1.58 S.D., 0.077 SEM), $t(390) = -22.3359$, $P < 0.0001$, and 6.1 (± 2.12 S.D., 0.109 S.E.M.), $t(380) = -29.7286$, $P < 0.0001$, respectively). No shift was observed when comparing Arc^{WT} to Arc^{s113-119A}, $t(390) = 3.6600$, $P > 0.0001$.

indicated by the paucity of Arc monomers and dimers in Arc mRNA-treated samples. Functionally, this raises the possibility that Arc mRNA could play a role in nucleating Arc interactions and promoting assembly toward virus-like capsids, but only the latter is dependent on the oligomerization motif. As mammalian Arc capsids contain Arc mRNA and possibly other cargoes, it will be important to determine whether the helical coil of the oligomerization region also functions in the internalization of mRNA.

Materials and methods

Plasmids

Human wild-type full-length Arc was cloned into the pETZZ_1a vector for expression in an N-terminal His-ZZ fusion tag and the rat Arc sequence with the s113-119A mutant was cloned into the pHMGWA vector, resulting in an N-terminal histidine and maltose-binding protein tag fused to the protein when expressed. TEV protease cleavage sites were located between the fusion tag and proteins to allow removal of the tag, leaving two extra residues (GA) and one extra residue (S) on the N-terminal side of the wild-type and mutant protein, respectively. The Arc constructs used for single-molecule photobleaching experiments were constructed with an N-terminal SUMO-His tag for purification, followed by a SNAP tag (SNAP26m) for labeling, and an AviTag at the C-terminal end for biotinylation. Gibson assembly was used to clone mutant Arc s113-119A. The FRET sensors used were described previously [31], all behind the cytomegalovirus promoter. Other plasmids encoding GST-fused or fluorescent protein-fused Arc fragments were

obtained by subcloning corresponding Arc fragments in pGEX-4T-3 (GE Healthcare Life Sciences) or FRET sensor plasmids between BamHI and NotI restriction sites. Plasmids encoding StrepII-tagged Arc fragments were generated from FRET sensors by substituting C-terminal fluorescent protein with StrepII-encoding oligo (GCGGCCGC-A-TCC GGA-TGGAGCCACCCGCAGTTCGAGAAA-GGT-GGA-GGT-TCC-GGA-GGT-GGA-TCG-GGA-GGT-GGA-TCG-TGGAGCCACCCGCAGTTCGAAAAA-GGT-TAA-CTC GAG) between NotI and XhoI restriction sites. Mutagenesis was performed using QuikChange Lightning Multi Site-Directed Mutagenesis Kit (Agilent, Santa Carla, CA, USA) according to the manufacturer's instructions. All constructs were verified by sequencing.

Protein expression and purification

All constructs were transformed into BL21 competent cells (Agilent) for IPTG-induced protein expression.

GST-fused Arc and GST

Cells were lysed in 100 mM NaCl, 10 mM Tris/HCl (pH 8.0), 1 mM EDTA, and 1% Triton X-100 (v/v). Cleared lysates were incubated with Glutathione Sepharose beads (GE Healthcare Life Sciences, Cytiva, Sheffield, UK) for 2 h, beads were washed, and bound protein eluted with 10 mM reduced glutathione. Samples were dialyzed overnight against 20 mM Tris/HCl (pH 7.4) and 150 mM NaCl. Purity of proteins was checked by separation on SDS gels and staining with InstantBlue protein stain (Merck, Saint-Louis, MO, USA) before measuring concentration with a NanoDrop Spectrophotometer (Thermo Fisher Scientific, Waltham, MA, USA).

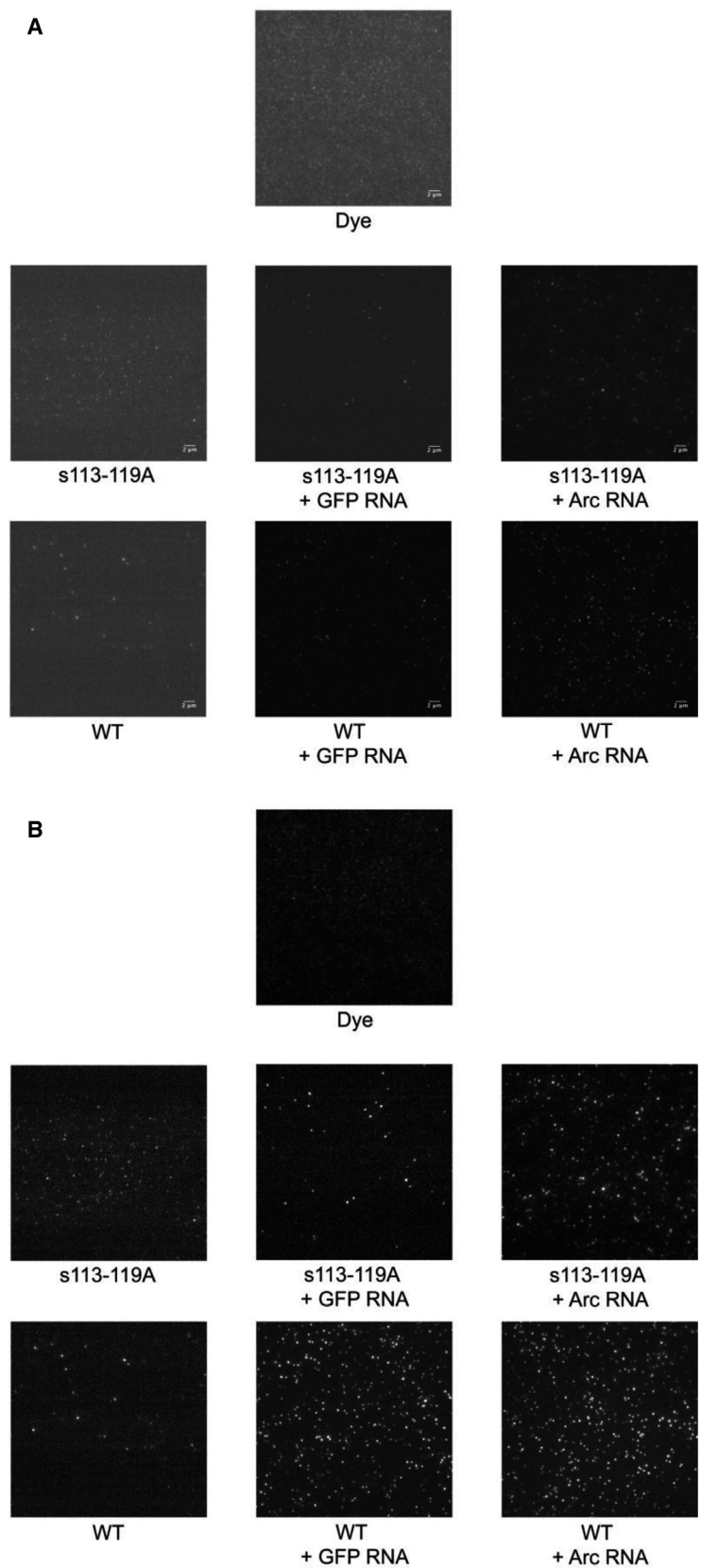


Fig. 10. Images from single-molecule TIRF prior to photobleaching. (A) Images adjusted to the same lookup table (LUT, 90-425). Scale bar = 2 μm . (B) LUTs were adjusted to maximize contrast for comparison purposes. Dye molecule spots have one fluorophore per molecule and are therefore the dimmest, which is why they are only clearly seen in the adjusted image. Nearly all molecules seen in the WT Arc + GFP or Arc mRNA samples were considered higher-order oligomers (i.e., brighter spots). Same scale bar from A applies here.

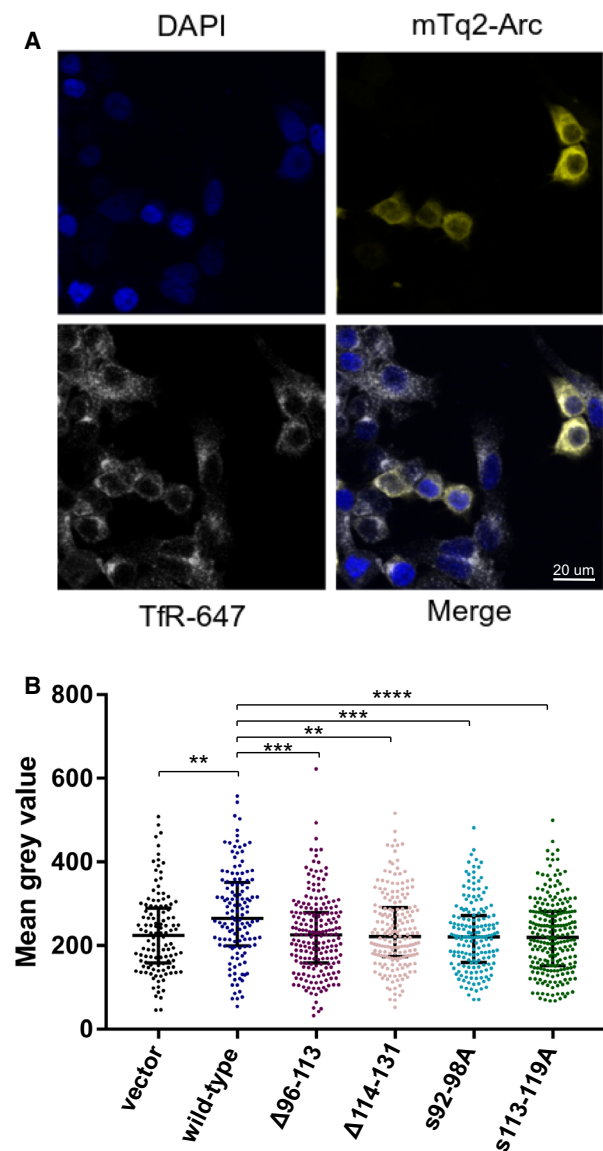


Fig. 11. Mutation of Arc oligomerization motif blocks transferrin endocytosis in HEK293FT cells. (A) Representative images of transferrin (TfR-647) uptake assay in HEK293FT cells transfected with mTq2-Arc (expression levels were similar across constructs). Nuclei stained by DAPI. Scale bar = 20 μm . (B) Quantification of transferrin uptake in HEK293FT cells represented as mean gray value. Scatter plot with lines indicating median and interquartile range. Kruskal–Wallis test between groups with Dunn’s multiple comparisons post hoc correction. * $P < 0.005$, *** $P < 0.0005$, **** $P < 0.0001$ to wild-type. $N = 3$, $n = 125, 132, 206, 190, 172$, and 229 , for empty vector, WT, $\Delta 96-113$, $\Delta 114-131$, s92-98A, and s113-119A, respectively.

Purification of Arc for smTIRF

Cells were lysed in 25 mM Tris pH 8.5, 150 mM KCl, 1 mM DTT, and 50 mM imidazole. Supernatant was filtered and loaded onto a 5 mL Ni-NTA column (all purification reagents were purchased from GE Healthcare Life Sciences). The protein was eluted by using 25 mM Tris, 50 mM KCl, 1 mM DTT, and 500 mM imidazole. The SUMO-His tag was cleaved by adding Ulp1 protease overnight at 4 $^{\circ}\text{C}$ and the sample desalted using TC (20 mM Tris pH 7.5, 125 mM NaCl, 2 mM TCEP) on a 26/10 desalting column. The sample was loaded onto a Q-FF 5-mL column and eluted using a gradient of NaCl. The sample was then run over an Superdex 200 size-exclusion column in Buffer C.

Purification of Arc for DLS and negative-stain EM

Full-length human Arc was expressed in *E. coli* and purified mainly as previously reported [19] with modifications (to be published). After TEV cleavage, protein was buffer-exchanged into 20 mM phosphate (pH 7) using a PD10 column.

Purification of Arc^{s113-119A} for SEC-MALS, DLS, SAXS, and EM

Cells were harvested, washed with a solution of 100 mM Tris/HCl (pH 7.5) and 170 mM NaCl, lysed in a buffer containing 40 mM HEPES (pH 7.5), 100 mM NaCl, 1 mM DTT, and 0.1 $\text{g}\cdot\text{L}^{-1}$ lysozyme by one freeze–thaw cycle followed by sonication. The lysed cells were centrifuged at 16 000 g for 30 min at 4 $^{\circ}\text{C}$, and the supernatant was loaded onto a Ni-NTA resin. The His-tagged protein was eluted using imidazole, treated with recombinant TEV protease, and dialyzed against 20 mM HEPES (pH 7.5), 100 mM NaCl, and 1 mM DTT for 16 h at 4 $^{\circ}\text{C}$. The now tagless protein was passed through the Ni-NTA resin again before purification by size-exclusion chromatography, using a Superdex 200 16/600 (GE Healthcare Life Sciences) column equilibrated with 20 mM Tris/HCl (pH 7.4) and 150 mM NaCl. The protein of interest gave one homogeneous peak which was collected and DTT was added to a final concentration of 1 mM. The protein sample was then concentrated using a 10 kDa MWCO spin concentrator to 4.4 $\text{mg}\cdot\text{mL}^{-1}$. The protein concentration was determined by absorbance measurements at 280 nm.

Commercial proteins and mRNA

A peptide of human Arc amino acids 99–132 (Ac-QETIANLERWVKREMHVWREVFYRLERWADRLES-OH) and a peptide array of partially overlapping peptides derived from rat Arc (NP_062234.1:71-147) were synthesized by INTAVIS Bioanalytical Instruments. Purified *in vitro* transcribed CleanCap EGFP mRNA and rat Arc mRNA were purchased from TriLink BioTechnologies (San Diego, CA, USA). The mRNAs contained the coding sequence and a 120 nucleotide polyA tail.

Peptide array

The peptide array was activated in methanol, washed in Tris-buffered saline with Tween (TBST: 50 mM Tris/HCl (pH 7.5), 150 mM NaCl, 0.1% (v/v) Tween 20), and blocked in TBST + 1% BSA (w/v). The array was first incubated with 0.5 $\mu\text{g}\cdot\text{mL}^{-1}$ purified GST for 1 h at room temperature, washed three times in TBST, and electrotransferred to nitrocellulose membrane using the Trans Blot Turbo transfer system (Bio-Rad Laboratories, Hercules, CA, USA). After transfer, the array was stripped in regeneration buffer (62.5 mM Tris/HCl (pH 6.7) + 2% SDS (w/v)) for 30 min, washed three times in TBST, and blocked before the second round of incubation with 0.5 $\mu\text{g}\cdot\text{mL}^{-1}$ GST-fused Arc 78–140 followed by electrotransfer. Transferred proteins were detected by an anti-GST antibody by western blotting using Pierce ECL Western Blotting Substrate (Thermo Fisher Scientific) according to the manufacturer's instructions.

Size-exclusion chromatography–multi-angle light scattering

The absolute molecular mass of the Arc^{s113–119A} mutant was determined with SEC-MALS, using a miniDAWN TREOS MALS detector. The SEC columns used were a Superdex 75 Increase 10/300 for the peptide and a Superdex 200 Increase 10/300 for the Arc^{s113–119A} mutant. The running buffer consisted of 20 mM Tris/HCl (pH 7.6) and 150 mM NaCl. The SEC-MALS system was calibrated with bovine serum albumin. The protein concentration was measured with an online refractometer.

Circular dichroism spectroscopy

The ellipticity of Arc peptide 99–132 was recorded using a Jasco J-810 Spectropolarimeter (JASCO, Easton, MD, USA) and a 1-mm quartz cuvette. The protein concentration was 0.2 $\text{g}\cdot\text{L}^{-1}$ in a buffer consisting of 20 mM phosphate (pH 7.6). The measurements were done at + 20 °C.

Dynamic light scattering

The hydrodynamic diameter of Arc^{WT} and Arc^{s113–119A} was measured using dynamic light scattering (DLS) at

1 $\text{mg}\cdot\text{mL}^{-1}$ at 4 °C in the 20 mM phosphate (pH 7) and 20 mM Tris/HCl (pH 7.6) and 150 mM NaCl, respectively. A Malvern Zetasizer Nano ZS with a He-Ne laser at 633 nm was used with a fixed scattering angle of 173°. The Malvern DTS software was used to evaluate the intensity and volume size distributions.

Small-angle X-ray scattering

Small-angle X-ray scattering data for purified recombinant nontagged Arc^{s113–119A} were collected on the B21 beamline at Diamond (Oxfordshire, UK) and on the SWING beamline at SOLEIL (Gif-sur-Yvette, France) for the MBP-tagged s113–119A mutant protein. A SEC-SAXS setup was used, and SAXS frames were collected as the protein eluted from a SEC column. The columns used were Shodex KW404-4F at Diamond and an Agilent ProSEC-300S at SOLEIL. The running buffer was 20 mM Tris/HCl (pH 7.4) with 150 mM NaCl. The protein concentration was 8 $\text{mg}\cdot\text{mL}^{-1}$ for the untagged protein and 20 $\text{mg}\cdot\text{mL}^{-1}$ for the MBP-tagged protein. All SAXS measurements were done at + 10 °C. SAXS data were processed using ATSAS [54], and the collected frames were checked to avoid radiation damage. SAXS models were generated using DAMMIN [55], DAMMIF [56], and GASBOR [57].

Crystallization and structure determination

The peptide containing human Arc residues 99–132 was at 13 $\text{mg}\cdot\text{mL}^{-1}$ in 20 mM Tris/HCl (pH 7.4), 150 mM NaCl. The peptide was crystallized in 45% MPD, 0.1 M Tris/HCl (pH 7.5) at + 8 °C, using sitting-drop vapor diffusion.

Crystals were snap-frozen in liquid nitrogen, and data collection was carried out at 100 K on the P13 beamline [58], PETRA III synchrotron storage ring, at EMBL/DESY, Hamburg, Germany. For S-SAD phasing using the anomalous signal from the single Met residue in the peptide, a dataset comprising 720° of rotation was collected at a wavelength of 2.066 Å, while a high-resolution native dataset was collected at 0.9796 Å from the same crystal. The SAD dataset was automatically processed during data collection with autoPROC [59], while native data were manually processed using XDS [60].

S-SAD phasing was performed using the AutoRickshaw pipeline [61]. The obtained 2.0-Å model was fully refined at 0.95-Å resolution using the native dataset in phenix.refine [62], and manual rebuilding was done in Coot [63]. The structure quality was assessed using MolProbity [64]. Electrostatics were calculated with APBS [65].

Data collection and refinement parameters are given in Table 1. The coordinates and structure factors were deposited at the Protein Data Bank with the entry code 6YTU. Raw data images, as well as the original processing files, for the SAD and native datasets are available at Zenodo,

Table 1. Crystallographic data collection and refinement

Dataset	S-SAD	Native
Data collection		
Wavelength (Å)	2.0664	0.9796
Unit cell parameters	a = 26.88 Å, b = 42.63 Å, c = 67.43 Å	a = 26.85 Å, b = 42.56 Å, c = 67.36 Å
Space group	P2 ₁ 2 ₁ 2 ₁	
Resolution range (Å)	100 – 1.94 (2.04 – 1.94)	100 – 0.95 (0.97 – 0.95)
Completeness (%)	86.9 (31.7)	90.7 (38.0)
$\langle I/\sigma \rangle$	58.2 (15.2)	18.7 (1.0)
R _{sym} (%)	4.3 (11.3)	8.1 (128.2)
R _{meas} (%)	4.4 (12.1)	8.5 (145.5)
CC _{1/2} (%)	99.9 (98.9)	99.9 (38.4)
Redundancy	20.5 (8.0)	10.8 (4.3)
Structure refinement and validation		
R _{cryst} (%)	-	10.3
R _{free} (%)	-	12.4
Rmsd bond length (Å)	-	0.020
Rmsd bond angle (°)	-	1.7
Ramachandran favoured (%)	-	100.0
MolProbity score/percentile	-	1.73 (39 th)

(<http://doi.org/10.5281/zenodo.3765570>; <http://doi.org/10.5281/zenodo.3766064>).

Single-molecule TIRF (total internal reflection fluorescence)

Coverslip preparation

Single-molecule experiments were performed as previously described [66,67]. Briefly, the Attofluor cell chamber (Thermo Fisher, Waltham, MA, USA) and glass coverslips were washed and sonicated in 1% Hellmanex, and then washed and sonicated again in 50% isopropanol. On the day of the experiment, the coverslips were plasma cleaned and then secured into the Attofluor cell chambers. 250 µL of PEG-Biotin/ PEG-PLL solution was added to the coverslip and incubated for 30 min. The coverslips were washed in 1x PBS. 250 µL streptavidin (10 mg·mL⁻¹) was added and incubated for 30 min. The coverslips were then washed in 20 mM Tris (pH 7.5), 125 mM NaCl, and 2 mM TCEP and incubated for another 10 min.

Sample preparation

Purified Arc was labeled with SNAP Alexa Fluor 488 dye (Thermo Fisher). The dye was added to the protein in 2X

molar excess and allowed to react in the dark for 1 h at RT. The sample was then desalted into Buffer C using a PD25 column. For experiments without mRNA addition, Alexa Fluor 488-labeled Arc was diluted to 3 nM in Buffer C and added onto the prepared coverslip. After a 1 min of incubation, the coverslip was washed 7x with Buffer C and an oxygen scavenger was added to the coverslip (5% glucose, 0.5 mg·mL⁻¹ glucose oxidase, 40 mg·mL⁻¹ catalase). For experiments with mRNA, 5 µM Arc was mixed with 0.1 mg·mL⁻¹ EGFP or Arc mRNA in RNase-free water for 2 h. The samples were then diluted and added to the prepared coverslip as above. For the Alexa dye control, a biotin-conjugated 488 dye (Biotium #80019) was dissolved in 25 mM Tris (pH 8.5) and diluted to 3 nM with PBS and added to prepared coverslips as above.

Single-molecule TIRF microscopy

The sample was imaged on the NSTORM/TIRF microscope housed in the UMass IALS Light Microscopy Facility. A total of 10 randomly chosen 1048x1048 pixel fields of view (164 × 164 µm) were imaged on each coverslip using the 488 nm laser at 30% power with an exposure time of 10 ms. Using the Nikon 100X Plan Apo TIRF objective and a Hamamatsu sCMOS camera, images were recorded for 15 s and no pixels were saturated.

Photobleaching analysis

TIRF images were analyzed using the NIS-Elements (Nikon, version 5.02) software package. First, each 15-second time-lapse series was cropped to include the first 5 s in order to attain maximum intensity projections. From these images, single particles (ROIs) were selected based on threshold, shape, and size using the General Analysis module. For the analysis of lower-order oligomers, a maximum intensity projection image in time was created over the first 5 s. The minimum threshold was 131 AU. Higher-order oligomers were selected by using the initial intensity of the first frame with a minimum intensity of 285. Intensities for each single particle were calculated over the trajectory of the 15 s of photobleaching time lapse. Fluorescence intensity vs. time plots were manually analyzed to (1) calculate representative step size and (2) discard traces with evidence of fluorophore blinking or irregular patterns such as single frame events or ROIs that had no initial intensity above baseline. The initial intensity for each ROI was calculated from averaging the first 50 time points. The baseline fluorescence was calculated by averaging the last 100 data points. Finally, the number of photobleaching steps was calculated using the following equation: (initial intensity-baseline intensity)/step size. Plots were generated using Prism 7. Independent 2-sample, one-tailed, *t*-tests were performed to compare between samples.

Electron microscopy and 3D single-particle reconstruction

Sample preparation

Purified Arc samples were subjected to SEC on a Superdex 200 10/300 GL column (GE Healthcare Life Sciences) equilibrated with PBS (pH 7.4). For the latter, 250 μ L fractions of the main peak (600–200 kDa) were collected and analyzed by EM. For negative-staining EM, carbon-coated 200-mesh copper/rhodium grids were glow discharged for 15 s in a vacuum chamber at 15 mA. 5 μ L samples were applied to the grids and incubated for 1 min, and excess sample was blotted with Whatman paper. Grids were washed with phosphate buffer once, then stained with 2% uranyl acetate, and blotted again to remove the excess contrast agent. Cryo-EM grids were prepared with a Vitrobot Mark IV (FEI) at 22 °C and 95% humidity. Aliquots of 4 μ L of the selected fractions were applied to a glow discharged holey carbon grid (QUANTIFOIL R2/2, 300 mesh), blotted for 1 s, and plunged into liquid ethane.

Negative-staining image acquisition and processing

For Arc^{WT}, images were taken using a Tecnai G2² FEG 200 (FEI) microscope operated at 200 kV and equipped with a 4k \times 4k FEI Eagle CCD camera at a nominal magnification of 50 000 \times . In the case of the Arc^{S113–119A}, images were taken using a JEOL 1010 JEM electron microscope operated at 80kV and equipped with a CCD camera (4Kx4K TemCam-F416, TVIPS). Images were recorded at a 65 000 \times nominal magnification with a pixel size of 15.50 μ m (2.4 Å /px sampling rate). These images were processed following the Scipion processing workflow [68]. Images were CTF-corrected using CTFFIND4 [69]. A total of 55,057 particles were automatically selected using Xmipp and 2D-classified using Relion 2.0 [70]. Some of the best classes were used as a template to build an initial model using RANSAC [71]. This model was filtered to 60 Å and used for refinement with Relion 3D auto-refine of the 28871 particles selected from the 2D classification, rendering a 21 Å resolution model. The apparent C2 symmetry of this first model was confirmed by applying this symmetry in the auto-refine process, after which a 3D reconstruction with a similar shape and resolution was generated. Visualization of the 3D models and docking of the atomic structures into EM volumes was performed manually using UCSF Chimera [72].

Cryo-EM image acquisition

Cryo-EM data were collected on a Thermo Fisher Talos Arctica transmission electron microscope operating at 200 kV. Images were acquired using a Falcon III direct electron detector, operated in electron counting mode at

73 000 \times nominal magnification (1.37 Å /pixel), with a nominal defocus range of -1.0 to -3.0 μ m.

Cell culture, hippocampal slice-culture preparation, and transfection

HEK293FT cells (R70007, Thermo Fisher Scientific) were grown in Dulbecco's modified Eagle's medium supplemented with 10% FBS and penicillin/streptomycin (Sigma-Aldrich, St. Louis, MO, USA) at 37 °C in a humidified incubator with 5% CO₂. For imaging studies, cells were plated on poly-L-lysine-coated coverslips. Cells were transfected using LipofectamineTM 2000 Transfection Reagent (Thermo Fisher Scientific) according to the manufacturer's instructions. Transverse hippocampal slice cultures were prepared from Sprague Dawley rats as described before at P8-10 and maintained for 7–10 days before transfection [31]. Ballistic DNA transfection was performed using a Gene Gun (Helios); 1.6- μ m gold microcarriers (Bio-Rad Laboratories) were coated with plasmid DNA and fired directly into individual wells in 6-well culture dishes containing hippocampal slices.

Affinity purification assay

About 24 h after transfection, cells were washed in ice-cold PBS and lysed in buffer containing 25 mM Tris/HCl (pH 7.4), 150 mM NaCl, 1 mM EDTA, 0.5 mM DTT, 0.5% Triton X-100 (vol/vol), cOmplete Mini Protease Inhibitor Tablets, and PhosSTOP Phosphatase Inhibitor Cocktail Tablets (Sigma-Aldrich). After centrifugation, 40 μ L of Strep-Tactin Sepharose (IBA Lifesciences, Göttingen, Germany) was added to the lysate followed by incubation for 1 h at 4 °C. Beads were washed in lysis buffer and immobilized proteins eluted by boiling in Laemmli sample buffer prior to separation on polyacrylamide gels by SDS/PAGE and immunoblotting. Probing of membranes with Strep-Tactin®-HRP conjugate was performed according to the manufacturer's instructions.

In situ protein cross-linking

Transfected HEK293FT cells were harvested in PBS and incubated for 10 min with the chemical cross-linking reagent disuccinimidyl glutarate (DSG, Sigma-Aldrich), dissolved in DMSO to a final concentration of 0.1 mM. The reaction was quenched with Tris (pH 7.5) for 10 min. Cells were lysed in buffer containing 60 mM HEPES (pH 7.5), 150 mM NaCl, 1 mM EDTA, 1 mM DTT, and cOmplete Mini Protease Inhibitor for 20 min at 4 °C. Protein concentrations of cleared lysates were determined with the PierceTM BCA Protein Assay Kit (Thermo Fisher Scientific), and the same amounts of protein were loaded prior to SDS/PAGE and immunoblotting. The intensity of bands was measured with ImageJ. One-way ANOVA with Bonferroni multiple comparison was used for statistical analysis.

Antibodies

Primary antibodies are as follows: mouse anti-GFP (B-2) (sc-9996, Santa Cruz Biotechnology, Dallas, TX, USA), Strep-Tactin®-HRP conjugate (Cat. No: 2-1502-001, IBA Lifesciences), mouse anti-Arc (C7) (sc-17839; Santa Cruz Biotechnology), and goat anti-GST (27-4577-01, GE Healthcare Life Sciences). Secondary antibodies are as follows: HRP-conjugated anti-mouse (cat. no: 401253-2) and anti-goat (sc-2020) antibodies from Merck.

Transferrin uptake assay and image analysis

HEK293FT cells plated on poly-L-lysine-coated coverslips were serum-starved for 4 h and placed on ice for 10 min prior to incubation with 15 $\mu\text{g}\cdot\text{mL}^{-1}$ Transferrin-AF647 (Thermo Fisher Scientific) for 15 min at 37 °C. Cells were washed and subsequently fixed in 4% PFA before mounting in ProLong Gold with DAPI (Thermo Fisher Scientific). Images were acquired on a Leica SP5 confocal microscope with a 40x objective. Settings were kept constant for each sample. Acquired stacks were analyzed by a custom-written macro in ImageJ. In brief, channels were split and used to create binary masks for transfected and nontransfected cells. Individual transfected cells were segmented using the watershed algorithm, and their masks were created using ‘Analyze Particles’ function. All images were manually checked after the automated analysis to exclude overlay masks for overlapping transfected and non-transfected cells. Intensity measurements for every channel were then performed for every transfected cell. Statistical significance between samples was tested by Kruskal–Wallis with Dunn’s multiple comparisons post hoc correction after normalization tests. The ImageJ macro is available upon request.

FLIM-FRET imaging

Imaging and data analysis were performed as described previously [31], with the same positive and negative controls for FRET. Briefly, two-photon FLIM-FRET imaging was performed on an Olympus FV1000 with an SPC-830 (Becker & Hickl) photon counting board for time-correlated single-photon counting. Photons were counted for 10–20 s, depending on expression level, in 64×64 pixels. The donor (EGFP) was excited using a 910-nm 2-photon laser (Spectra-Physics), and emission was captured in an H7422-40 detector (Hamamatsu). Fluorescence lifetime was calculated in SPC-image software (Becker & Hickl), using mono-exponential curve fitting of photon distributions.

Secondary structure predictions

In silico secondary structure predictions were performed using the COILS (10) and JPred (11) servers.

Acknowledgments

This work was supported by a Research Council of Norway Toppforsk grant (249951) to CRB, grant PID2019-105872GB-I00/AEI/10.13039/501100011033 (AEI/FEDER, UE) to JMV, and grant MEXT, Japan (20240032, 16H02455, 22110006, 18H04733, and 18H05434), to Y.H. TIRF imaging was performed in the Light Microscopy Facility and Nikon Center of Excellence at the Institute for Applied Life Sciences, University of Massachusetts Amherst, with support from the Massachusetts Life Science Center. We gratefully acknowledge beamtime and beamline support at Diamond Light Source, EMBL/DESY, and SOLEIL.

Author contributions

MSE, ON, and CRB conceived the study. MSE performed cloning and affinity purification assays, protein purification, transferrin uptake assays, confocal imaging, and image analysis. ON performed cloning and affinity purification assays and wrote the ImageJ macro. SG, TH, and YH performed FLIM-FRET imaging and analysis. DL, SA, and TK performed the cross-linking experiments and analysis. RO, JJC, IM, and MMS designed and performed the single-molecule imaging experiments. HJB, MIF, and AM prepared human recombinant Arc for EM imaging and performed DLS analysis. JC and JMV performed EM imaging and 3D reconstruction analysis. EIH and PK performed protein purifications, CD spectroscopy, SEC-MALS, SAXS, and crystallography, with contributions from CT on the latter. GM and RL performed SAXS on MBP-Arc. MSE and CRB wrote the paper with contributions from all authors.

Conflict of interest

The authors declare no conflict of interest.

Peer Review

The peer review history for this article is available at <https://publons.com/publon/10.1111/febs.15618>.

References

- 1 Zhang H & Bramham CR (2020) Arc/Arg3.1 function in long-term synaptic plasticity: emerging mechanisms and unresolved issues. *Eur J Neurosci* **ejn.14958**.
- 2 Shepherd JD & Bear MF (2011) New views of Arc, a master regulator of synaptic plasticity. *Nat Neurosci* **14**, 279–284.

- 3 Bramham CR, Alme MN, Bittins M, Kuipers SD, Nair RR, Pai B, Panja D, Schubert M, Soule J, Tiron A *et al.* (2010) The Arc of synaptic memory. *Exp Brain Res* **200**, 125–140.
- 4 Chowdhury S, Shepherd JD, Okuno H, Lyford G, Petralia RS, Plath N, Kuhl D, Haganir RL & Worley PF (2006) Arc/Arg3.1 interacts with the endocytic machinery to regulate AMPA receptor trafficking. *Neuron* **52**, 445–459.
- 5 Korb E, Wilkinson CL, Delgado RN, Lovero KL & Finkbeiner S (2013) Arc in the nucleus regulates PML-dependent GluA1 transcription and homeostatic plasticity. *Nat Neurosci* **16**, 874–883.
- 6 DaSilva LLP, Wall MJ, de Almeida P, Wauters SC, Januário YC, Müller J & Corrêa SAL (2016) Activity-regulated cytoskeleton-associated protein controls AMPAR endocytosis through a direct interaction with Clathrin-Adaptor Protein 2. *eneuro* **3**, ENEURO.0144.
- 7 Okuno H, Akashi K, Ishii Y, Yagishita-Kyo N, Suzuki K, Nonaka M, Kawashima T, Fujii H, Takemoto-Kimura S, Abe M *et al.* (2012) Inverse synaptic tagging of inactive synapses via dynamic interaction of Arc/Arg3.1 with CaMKII. *Cell* **149**, 886–898.
- 8 Nair RR, Patil S, Tiron A, Kanhema T, Panja D, Schiro L, Parobczak K, Wilczynski G & Bramham CR (2017) Dynamic Arc SUMOylation and selective interaction with F-actin-binding protein drebrin in LTP Consolidation in vivo. *Front Synaptic Neurosci* **9**. <https://doi.org/10.3389/fnsyn.2017.00008>
- 9 Zhang W, Wu J, Ward MD, Yang S, Chuang Y-A, Xiao M, Li R, Leahy DJ & Worley PF (2015) Structural basis of Arc binding to synaptic proteins: implications for cognitive disease. *Neuron* **86**, 490–500.
- 10 Nikolaienko O, Patil S, Eriksen MS & Bramham CR (2018) Arc protein: a flexible hub for synaptic plasticity and cognition. *Semin Cell Dev Biol* **77**, 33–42.
- 11 Craig TJ, Jaafari N, Petrovic MM, Rubin PP, Mellor JR & Henley JM (2012) Homeostatic synaptic scaling is regulated by protein SUMOylation. *J Biol Chem* **287**, 22781–22788.
- 12 Nikolaienko O, Eriksen MS, Patil S, Bito H & Bramham CR (2017) Stimulus-evoked ERK-dependent phosphorylation of activity-regulated cytoskeleton-associated protein (Arc) regulates its neuronal subcellular localization. *Neuroscience* **360**, 68–80.
- 13 Gozdz A, Nikolaienko O, Urbanska M, Cymerman IA, Sitkiewicz E, Blazejczyk M, Dadlez M, Bramham CR & Jaworski J. (2017) GSK3 α and GSK3 β phosphorylate arc and regulate its degradation. *Front Mol Neurosci* **10**. <https://doi.org/10.3389/fnmol.2017.00192>
- 14 Greer PL, Hanayama R, Bloodgood BL, Mardinly AR, Lipton DM, Flavell SW, Kim TK, Griffith EC, Waldon Z, Maehr R *et al.* (2010) The Angelman Syndrome protein Ube3A regulates synapse development by ubiquitinating arc. *Cell* **140**, 704–716.
- 15 Mabb AM, Je HS, Wall MJ, Robinson CG, Larsen RS, Qiang Y, Corrêa SAL & Ehlers MD (2014) Triad3A regulates synaptic strength by ubiquitination of Arc. *Neuron* **82**, 1299–1316.
- 16 Lalonde J, Reis SA, Sivakumaran S, Holland CS, Wesseling H, Sauld JF, Alural B, Zhao W-N, Steen JA & Haggarty SJ (2017) Chemogenomic analysis reveals key role for lysine acetylation in regulating Arc stability. *Nat Commun* **8**, 1659.
- 17 Wall MJ, Collins DR, Chery SL, Allen ZD, Pastuzyn ED, George AJ, Nikolova VD, Moy SS, Philpot BD, Shepherd JD *et al.* (2018) The temporal dynamics of Arc expression regulate cognitive flexibility. *Neuron* **98**, 1124–1132.e7.
- 18 Byers CE, Barylko B, Ross JA, Southworth DR, James NG, Taylor CA, Wang L, Collins KA, Estrada A, Waung M *et al.* (2015) Enhancement of dynamin polymerization and GTPase activity by Arc/Arg3.1. *Biochim Biophys Acta* **1850**, 1310–1318.
- 19 Myrum C, Baumann A, Bustad HJ, Flydal MI, Mariaule V, Alvira S, Cuéllar J, Haavik J, Soulé J, Valpuesta JM *et al.* (2015) Arc is a flexible modular protein capable of reversible self-oligomerization. *Biochem J* **468**, 145–158.
- 20 Campillos M, Doerks T, Shah PK & Bork P (2006) Computational characterization of multiple Gag-like human proteins. *Trends Genet* **22**, 585–589.
- 21 Nielsen LD, Pedersen CP, Erlendsson S & Teilmann K (2019) The capsid domain of Arc changes its oligomerization propensity through direct interaction with the NMDA Receptor. *Structure* **27**, 1071–1081.e5.
- 22 Lingappa JR, Reed JC, Tanaka M, Chutiraka K & Robinson BA (2014) How HIV-1 Gag assembles in cells: Putting together pieces of the puzzle. *Virus Res* **193**, 89–107.
- 23 Perilla JR & Gronenborn AM (2016) Molecular architecture of the retroviral capsid. *Trends Biochem Sci* **41**, 410–420.
- 24 Ashley J, Cordy B, Lucia D, Fradkin LG, Budnik V & Thomson T (2018) Retrovirus-like Gag protein Arc1 binds RNA and traffics across synaptic boutons. *Cell* **172**, 262–274.e11.
- 25 Pastuzyn ED, Day CE, Kearns RB, Kyrke-Smith M, Taibi AV, McCormick J, Yoder N, Belnap DM, Erlendsson S, Morado DR *et al.* (2018) The neuronal gene Arc encodes a repurposed retrotransposon Gag protein that mediates intercellular RNA transfer. *Cell* **172**, 275–288.e18.
- 26 Shepherd JD (2018) Arc – An endogenous neuronal retrovirus? *Semin Cell Dev Biol* **77**, 73–78.

- 27 Parrish NF & Tomonaga K (2018) A viral (Arc)hive for metazoan memory. *Cell* **172**, 8–10.
- 28 Cottee MA, Letham SC, Young GR, Stoye JP & Taylor IA (2020) Structure of *D. melanogaster* ARC1 reveals a repurposed molecule with characteristics of retroviral Gag. *Sci Adv* **6**, eaay6354.
- 29 Erlendsson S, Morado DR, Cullen HB, Feschotte C, Shepherd JD & Briggs JAG (2020) Structures of virus-like capsids formed by the *Drosophila* neuronal Arc proteins. *Nat Neurosci* **23**, 172–175.
- 30 Mailler E, Bernacchi S, Marquet R, Paillart J-C, Vivet-Boudou V & Smyth RP (2016) The life-cycle of the HIV-1 Gag-RNA complex. *Viruses* **8**, 248–266.
- 31 Hallin EI, Eriksen MS, Baryshnikov S, Nikolaienko O, Grødem S, Hosokawa T, Hayashi Y, Bramham CR & Kursula P (2018) Structure of monomeric full-length ARC sheds light on molecular flexibility, protein interactions, and functional modalities. *J Neurochem* **147**, 323–343.
- 32 Barylko B, Wilkerson JR, Cavalier SH, Binns DD, James NG, Jameson DM, Huber KM & Albanesi JP (2018) Palmitoylation and membrane minding of Arc/Arg3.1: a potential role in synaptic depression. *Biochemistry* **57**, 520–524.
- 33 Kelly BN, Howard BR, Wang H, Robinson H, Sundquist WI & Hill CP (2006) Implications for viral capsid assembly from crystal structures of HIV-1 Gag1-278 and CAN133-278. *Biochemistry* **45**, 11257–11266.
- 34 Dettmer U, Newman AJ, Luth ES, Bartels T & Selkoe D (2013) In vivo cross-linking reveals principally oligomeric forms of alpha-synuclein and alpha-synuclein in neurons and non-neural cells. *J Biol Chem* **288**, 6371–6385.
- 35 Ivanov D, Tsodikov OV, Kasanov J, Ellenberger T, Wagner G & Collins T (2007) Domain-swapped dimerization of the HIV-1 capsid C-terminal domain. *PNAS* **104**, 4353–4358.
- 36 Muriaux D, Mirro J, Harvin D & Rein A (2002) RNA is a structural element in retrovirus particles. *Proc Natl Acad Sci USA* **98**, 5246–5251.
- 37 Briggs JAG, Riches JD, Glass B, Bartonova V, Zanetti G & Krausslich H-G (2009) Structure and assembly of immature HIV. *Proc Natl Acad Sci USA* **106**, 11090–11095.
- 38 Pornillos O, Ganser-Pornillos BK, Kelly BN, Hua Y, Whitby FG, Stout CD, Sundquist WI, Hill CP & Yeager M (2009) X-Ray structures of the hexameric building block of the HIV capsid. *Cell* **137**, 1282–1292.
- 39 Zhang W, Chuang Y-A, Na Y, Ye Z, Yang L, Lin R, Zhou J, Wu J, Qiu J, Savonenko A *et al.* (2019) Arc oligomerization is regulated by CaMKII phosphorylation of the GAG domain: an essential mechanism for plasticity and memory formation. *Mol Cell* **75**, 13–25.e5.
- 40 Lu K, Heng X & Summers MF (2011) Structural determinants and mechanism of HIV-1 genome packaging. *J Mol Biol* **410**, 609–633.
- 41 Lingappa JR, Dooher JE, Newman MA, Kiser PK & Klein KC (2006) Basic residues in the nucleocapsid domain of Gag are required for interaction of HIV-1 Gag with ABCE1 (HP68), a cellular protein important for HIV-1 capsid assembly. *J Biol Chem* **281**, 3773–3784.
- 42 Burniston MT, Cimarelli A, Colgan J, Curtis SP & Luban J (1999) Human immunodeficiency virus type 1 Gag polyprotein multimerization requires the nucleocapsid domain and RNA and is promoted by the capsid-dimer interface and the basic region of matrix protein. *J Virol* **73**, 8527–8540.
- 43 Campbell S & Vogt VM (1997) In vitro assembly of virus-like particles with Rous sarcoma virus Gag deletion mutants: identification of the p10 domain as a morphological determinant in the formation of spherical particles. *J Virol* **71**, 4425–4435.
- 44 Campbell S & Rein A (1999) In vitro assembly properties of human immunodeficiency virus type 1 Gag protein lacking the p6 domain. *J Virol* **73**, 2270–2279.
- 45 Alfadhli A, Dhenub TC, Still A & Barklis E (2005) Analysis of human immunodeficiency virus type 1 Gag dimerization-induced assembly. *J Virol* **79**, 14498–14506.
- 46 Ma YM & Vogt VM (2004) Nucleic acid binding-induced Gag dimerization in the assembly of Rous Sarcoma virus particles in vitro. *J Virol* **78**, 52–60.
- 47 Zhang Y, Qian H, Love Z & Barklis E (1998) Analysis of the assembly function of the human immunodeficiency virus type 1 gag protein nucleocapsid domain. *J Virol* **72**, 1782–1789.
- 48 Crist RM, Datta SAK, Stephen AG, Soheilian F, Mirro J, Fisher RJ, Nagashima K & Rein A (2009) Assembly properties of human immunodeficiency virus type 1 Gag-leucine zipper chimeras: implications for retrovirus assembly. *J Virol* **83**, 2216–2225.
- 49 Johnson MC, Scobie HM, Ma YM & Vogt VM (2002) Nucleic acid-independent retrovirus assembly can be driven by dimerization. *J Virol* **76**, 11177–11185.
- 50 Gaines CR, Tkacik E, Rivera-Oven A, Somani P, Achimovich A, Alabi T, Zhu A, Getachew N, Yang AL, McDonough M *et al.* (2018) HIV-1 matrix protein interactions with tRNA: implications for membrane targeting. *J Mol Biol* **430**, 2113–2127.
- 51 Steward O & Worley PF (2001) Selective targeting of newly synthesized Arc mRNA to active synapses requires NMDA receptor activation. *Neuron* **30**, 227–240.
- 52 Panja D, Kenney JW, D'Andrea L, Zalfa F, Vedeler A, Wibrand K, Fukunaga R, Bagni C, Proud CG & Bramham CR (2014) Two-stage translational control of dentate gyrus LTP consolidation is mediated by

- sustained BDNF-TrkB signaling to MNK. *Cell Rep* **9**, 1430–1445.
- 53 Steward O, Farris S, Pirbhoy P, Darnell J & Van Driesche S (2015) Localization and local translation of Arc/Arg3.1 mRNA at synapses: some observations and paradoxes. *Front mol neurosci* **7**. <https://doi.org/10.3389/fnmol.2014.00101>
- 54 Franke D, Petoukhov MV, Konarev PV, Panjkovich A, Tuukkanen A, Mertens HDT, Kikhney AG, Hajizadeh NR, Franklin JM, Jeffries CM *et al.* (2017) ATSAS 2.8: A comprehensive data analysis suite for small-angle scattering from macromolecular solutions. *J Appl Crystallogr* **50**, 1212–1225.
- 55 Svergun DI (1999) Restoring low resolution structure of biological macromolecules from solution scattering using simulated annealing. *Biophys J* **76**, 2879–2886.
- 56 Franke D & Svergun DI (2009) DAMMIF, a program for rapid ab-initio shape determination in small-angle scattering. *J Appl Crystallogr* **42**, 342–346.
- 57 Svergun DI, Petoukhov MV & Koch MHJ (2001) Determination of domain structure of proteins from x-ray solution scattering. *Biophys J* **80**, 2946–2953.
- 58 Cianci M, Bourenkov G, Pompidor G, Karpics I, Kallio J, Bento I, Roessle M, Cipriani F, Fiedler S & Schneider TR (2017) P13, the EMBL macromolecular crystallography beamline at the low-emittance PETRA III ring for high- and low-energy phasing with variable beam focusing. *J Synchrotron Radiat* **24**, 323–332.
- 59 Vonrhein C, Flensburg C, Keller P, Sharff A, Smart O, Paciorek W, Womack T & Bricogne G (2011) Data processing and analysis with the autoPROC toolbox. *Acta Crystallogr Sect D Biol Crystallogr* **67**, 293–302.
- 60 Kabsch W. (2010) XDS. *Acta Crystallogr Sect D Biol Crystallogr* **66**, 125–132.
- 61 Panjikar S, Parthasarathy V, Lamzin VS, Weiss MS & Tucker PA (2005) Auto-Rickshaw: an automated crystal structure determination platform as an efficient tool for the validation of an X-ray diffraction experiment. *Acta Crystallogr Sect D Biol Crystallogr* **61**, 449–457.
- 62 Afonine PV, Grosse-Kunstleve RW, Echols N, Headd JJ, Moriarty NW, Mustyakimov M, Terwilliger TC, Urzhumtsev A, Zwart PH & Adams PD (2012) Towards automated crystallographic structure refinement with phenix.refine. *Acta Crystallogr Sect D Biol Crystallogr* **68**, 352–367.
- 63 Emsley P, Lohkamp B, Scott WG & Cowtan K (2010) Features and development of Coot. *Acta Crystallogr Sect D Biol Crystallogr* **66**, 486–501.
- 64 Davis IW, Leaver-Fay A, Chen VB, Block JN, Kapral GJ, Wang X, Murray LW, Arendall WB, Snoeyink J, Richardson JS *et al.* (2007) MolProbity: All-atom contacts and structure validation for proteins and nucleic acids. *Nucleic Acids Res* **35**, 375–383.
- 65 Jurrus E, Engel D, Star K, Monson K, Brandi J, Felberg LE, Brookes DH, Wilson L, Chen J, Liles K *et al.* (2018) Improvements to the APBS biomolecular solvation software suite. *Protein Sci* **27**, 112–128.
- 66 Stratton M, Lee I-H, Bhattacharyya M, Christensen SM, Chao LH, Schulman H, Groves JT & Kuriyan J (2014) Activation-triggered subunit exchange between CaMKII holoenzymes facilitates the spread of kinase activity. *Elife* **3**, 1–28.
- 67 Zhang H & Guo P (2014) Single molecule photobleaching (SMPB) technology for counting of RNA, DNA, protein and other molecules in nanoparticles and biological complexes by TIRF instrumentation. *Methods* **67**, 169–176.
- 68 de la Rosa-Trevín JM, Quintana A, del Cano L, Zaldívar A, Foche I, Gutiérrez J, Gómez-Blanco J, Burguet-Castell J, Cuenca-Alba J, Abrishami V *et al.* (2016) Scipion: A software framework toward integration, reproducibility and validation in 3D electron microscopy. *J Struct Biol* **195**, 93–99.
- 69 Rohou A & Grigorieff N (2015) CTFFIND4: Fast and accurate defocus estimation from electron micrographs. *J Struct Biol* **192**, 216–221.
- 70 Kimanius D, Forsberg BO, Scheres SHW & Lindahl E (2016) Accelerated cryo-EM structure determination with parallelisation using GPUs in RELION-2. *Elife* **5**, 1–21.
- 71 Vargas J, Álvarez-Cabrera A-L, Marabini R, Carazo JM & Sorzano COS (2014) Efficient initial volume determination from electron microscopy images of single particles. *Bioinformatics* **30**, 2891–2898.
- 72 Pettersen EF, Goddard TD, Huang CC, Couch GS, Greenblatt DM, Meng EC & Ferrin TE (2004) UCSF Chimera - A visualization system for exploratory research and analysis. *J Comput Chem* **25**, 1605–1612.